



Joint Yaw-Induction Control Optimization for Wind Farms

Kirby S. Heck^{1,*}, Jaime Liew^{1,*}, Ilan M. L. Upfal¹, and Michael F. Howland¹

¹Civil and Environmental Engineering, Massachusetts Institute of Technology, Cambridge, MA 02139, USA

*These authors contributed equally to this work.

Correspondence: Michael F. Howland (mhowland@mit.edu)

Abstract. Wind farm flow control has demonstrated significant potential to increase wind farm power and energy production. Two commonly used methods are wake steering, which entails yaw misaligning individual turbines to deflect wakes laterally, and induction control, which typically modifies the thrust coefficients of individual wind turbines to reduce wake deficits. These two control approaches are often studied and utilized independently. This study investigates the combination of both of these strategies, termed *joint yaw-induction control*. By synergistically controlling wind turbine yaw angles and thrust levels, increased wind power can be achieved compared to either induction or yaw control in isolation. This research leverages the Unified Momentum Model to capitalize on the interplay between the yaw misalignment and the thrust coefficient of a turbine rotor on the power and wake velocities generated by the wind turbine. The Unified Momentum Model is integrated with blade element modeling to yield a blade element momentum model that both predicts the power and forces on wind turbines with arbitrary input of yaw, pitch, and tip speed ratio, and also predicts the initial wake velocities needed for far-wake models. Forward-mode automatic differentiation is integrated into the rotor and wake model to efficiently optimize control strategies using gradient-based optimization. Using the fast-running wind farm model, which is a coupling between the Unified Momentum Model and a Gaussian far-wake model, we demonstrate that joint yaw-induction control outperforms individual yaw or thrust control strategies, leading to significant increases in power production. First using a two-turbine test case, we show that the Unified Momentum Model reliably predicts the dependence of the freestream turbine power on its yaw and thrust coefficient compared to 210 independent large eddy simulations of wind turbines in a conventionally neutral atmospheric boundary layer. However, larger discrepancies result from the wake model, particularly in yawed conditions. The leading turbine control strategy that maximizes the combined power of the two turbines entails yaw misalignment and a thrust coefficient larger than Betz-optimal. Next, a 25-turbine wind farm case study highlights the benefits of integrated rotor and wake modeling but indicates that improvements in fast-running, gradient-compatible wake models are required to realize the potential benefits of joint yaw-induction control. The findings underscore the importance of modeling interdependencies between yaw and induction control to inform effective optimization strategies.

1 Introduction

Wind energy, recognized as one of the most scalable carbon-neutral energy technologies alongside solar power, is considered a key player in the future of renewable energy systems (Shukla et al., 2022). Projections suggest that by 2050, wind power could account for up to a third of global electricity production (IEA, 2021; IRENA, 2022). However, with the anticipated rapid



growth in wind energy, the electricity market may face self-cannibalization effects, where the increased availability of wind energy leads to a decline in farm revenue (Prol et al., 2020; Peña et al., 2022). Consequently, periods of low wind speed, and thus low wind energy availability, are particularly valuable for increasing wind energy production because prices are higher during these times.

Wind farm flow control, a technique involving the manipulation of wind turbines to mitigate or redirect the adverse impacts of wakes within a wind farm, has attracted significant interest within the research community, particularly due to its added value in low wind speed conditions (Howland et al., 2019; Kölle et al., 2022). To benefit the collective wind farm, wind turbines can be controlled using different techniques to reduce the magnitude of wake deficits or to redirect the wakes away from turbines downwind (Kheirabadi and Nagamune, 2019; Meyers et al., 2022). One wind farm flow control approach is axial induction control, also known as thrust control, curtailment, or derating control, which involves reducing the thrust force of an upstream turbine, thereby decreasing the intensity of the wake it generates (Lio et al., 2018). Wake steering, also referred to as yaw steering or wake deflection control, entails intentionally misaligning the wind turbine from the incoming wind direction, causing the wake to deflect laterally as it propagates downstream (Jiménez et al., 2010; Gebraad et al., 2016). In both cases, the upstream turbines experience a power loss to potentially benefit the downstream turbines by exposing them to faster, less turbulent wind.

Both wake steering and induction control have demonstrated promising outcomes in terms of controlling wind farm power output (Kheirabadi and Nagamune, 2019; Houck, 2022) as well as potentially mitigating turbine structural loads (Croce et al., 2024). While wake steering has become the dominantly studied strategy among the two due to its benefits on farm power production increase (e.g. Meyers et al., 2022), several investigations advocate for the concurrent implementation of both yaw and induction control strategies (Munters and Meyers, 2018; Bossanyi, 2018; Debusscher et al., 2022). For example, Munters and Meyers (2018) solved the PDE-constrained optimization problem using large eddy simulations as the wind farm model and revealed the potential for combining overinductive axial induction control with yaw control to yield higher power gains than applying each strategy independently. However, to inform optimization strategies that rely on joint yaw and induction control, engineering wind farm models must reliably predict the coupled impacts of these control strategies on the upstream turbine and on the wake.

Existing studies and fast-running wind farm models often treat yaw control and induction control independently. However, varying the yaw angle changes the rotor thrust, which implicitly impacts the axial induction (Heck et al., 2023). Consequently, yaw control implicitly induces changes in axial induction control unless it is actively prevented. This change in induction has implications for the strength of the resultant wake and for the power losses attributed to yaw misalignment of the upstream turbine. Beyond the yaw angle, the blade pitch angle and the generator torque are two additional degrees of freedom governing the wind turbine control strategy. Standard approaches to modeling wind power in yaw misalignment assume that the power will decrease with $\cos^{P_p}(\gamma)$, where γ is the yaw misalignment angle and P_p is a turbine-specific tunable parameter (e.g., Gebraad et al., 2016). However, the power production of a wind turbine in yaw misalignment also depends on the pitch and torque control (Howland et al., 2020b; Tamaro et al., 2024). So even if a tuned exponent P_p was identified for a given turbine model, it would only be valid for a specific choice of how pitch and generator torque are modified when the yaw misalignment



is applied to the rotor (Tamaro et al., 2024; Liew et al., 2024b). Note that similar tunable parameters have also been defined for the dependence of the thrust force on the yaw misalignment angle (Bastankhah and Porté-Agel, 2017). The blade pitch and the generator torque, in combination with the turbine yaw angle, are the quantities that can be readily controlled on the wind turbine.

65 Therefore, these three variables constrain the degree to which the induction can be controlled. Modeling the interdependencies between wake deflection, thrust force, power, yaw, blade pitch, and generator torque is crucial for maximizing wind farm performance through coordinated flow control strategies.

Many studies exist on induction control in which the induction or rotor thrust is directly controlled in actuator disk simulations (Vitulli et al., 2019; Pedersen and Larsen, 2020). For a yaw aligned horizontal axis wind turbine, rotor thrust cannot
70 be directly controlled but is instead a result of the rotor speed, which can be non-dimensionalized as the tip speed ratio, and the blade pitch. Additionally, when translating the results from actuator disk modeling to more realistic rotor modeling (e.g. blade element modeling), different combinations of blade pitch and tip speed ratio may result in the same thrust coefficient. Induction control therefore has numerous potential strategies to navigate the two degrees of freedom to achieve a target power output. Two common derating strategies include maintaining a constant rotor speed (tip speed ratio) or blade pitch angle; an
75 alternative derating approach minimizes the thrust coefficient for a target power output (Lio et al., 2018; Juangarcia et al., 2018). In the context of maximizing wind farm power, the minimum thrust derating strategy has the additional co-benefit of minimizing wake effects, and therefore has been shown to be a useful method for derating (Vitulli et al., 2019; Pedersen and Larsen, 2020).

Existing research has primarily examined derating/induction control in isolation. When incorporating wake steering, the
80 determination of the minimum thrust trajectory becomes more intricate due to the introduction of a third interrelated variable: the yaw misalignment angle. This complexity and its implications were investigated by Liew et al. (2024b) in a study highlighting the coupled effects of performing a combination of yaw control and thrust control. In general, Liew et al. (2024b) identified that the minimum thrust trajectory set points for the tip speed ratio and blade pitch angle vary with yaw angle. This means that a yawed turbine operating at the minimum thrust set point as determined by a yaw-aligned turbine will be operating
85 sub-optimally in terms of both power maximization and thrust minimization objectives. Recent studies that have investigated co-benefits of yaw and thrust control have done so using empirical frameworks for the aerodynamic performance of the rotor and/or characteristics of the wake (Zhang et al., 2024; Hosseini et al., 2025). Because empirical models of power and thrust variations in yaw misalignment rely on calibrated parameters that depend on the rotor control strategy, extrapolating these empirical models out-of-sample to arbitrary control strategies incurs error and uncertainty (Howland et al., 2020b).

90 We address the optimization of wind farm control through the utilization of both yaw and thrust (derating) control. This is made possible by leveraging the physics-based rotor aerodynamic modeling introduced by Heck et al. (2023) and later expanded by Liew et al. (2024a) in the Unified Momentum Model, which captures the combined dynamics of turbine induction (blade pitch and tip speed ratio) and yaw on turbine power and thrust. In tandem, the Unified Momentum Model also predicts the initial streamwise and lateral wake velocities that are consistent with the thrust and power of the rotor. These velocities are naturally
95 coupled to turbulent far-wake models, such as the widely-used Jensen (Jensen, 1983) or Gaussian (Bastankhah and Porté-Agel, 2014) wake models. The Unified Momentum Model facilitates computationally efficient rotor modeling, particularly in yaw-



misaligned conditions and for both low and high thrust regimes without relying on empirically tuned cosine models, skewed wake corrections, or high thrust corrections (Liew et al., 2024a). This generalization of classical one-dimensional momentum theory is critical to enabling the accurate and efficient joint yaw-induction control of wind farms.

100 In this study, we develop a wind farm modeling and optimization framework that combines engineering rotor and wake modeling with efficient, analytical, gradient-based control optimization using automatic differentiation. The wind farm model combines the Unified Momentum rotor model with a Gaussian engineering wake model to predict the turbulent far-wake. We design and implement a forward-mode automatic differentiation algorithm using dual numbers to efficiently solve constrained optimization problems aimed at maximizing collective wind farm power production. The analytical gradient calculations are
105 demonstrated with both actuator disk and blade element momentum (BEM) rotor modeling. To quantify the increase in energy production via joint yaw-induction control compared to thrust or yaw control in isolation, we first perform optimization case studies using the engineering model and then we verify the engineering model findings using large eddy simulations (LES). We consider two case studies: a two-turbine wind turbine array and a larger 25-turbine, grid-layout wind farm. In these case studies, both the actuator disk and BEM models are used and compared within the engineering wind farm model. The actuator
110 disk model optimization allows us to understand the optimum control strategy for an idealized turbine that can achieve any combination of thrust and yaw and produces power according to its thrust force and rotor-normal wind speed. In contrast, the BEM model, based on the Unified Momentum Model (Liew et al., 2024a), captures the limitations on thrust and yaw due to blade aerodynamics, as well as the impact of computing power from rotor angular velocity and torque, which can account for losses. By comparing thrust, yaw, and joint yaw-induction wind farm control strategies, we demonstrate the benefits of
115 joint yaw-induction control relative to each approach applied individually. Furthermore, we compare our findings from the engineering wind farm model with LES of actuator disk-modeled wind turbines in atmospheric boundary layer conditions for both the two-turbine and 25-turbine cases. To conclude, we identify opportunities to enhance wind farm control optimization in future work.

The remainder of this article is organized as follows. In Sect. 2, we introduce the rotor momentum model, blade element
120 model, turbulent far-wake model, automatic differentiation algorithm, and the LES numerical setup. Then, in Sect. 4.1, we highlight results from the wind farm model using a two-turbine wind farm. These results are compared with LES of the same two-turbine wind farm simulated across a full range of control conditions at one wind direction. Next, in Sect. 4.2, we analyze a larger 25-turbine wind farm. A discussion follows in Sect. 5, followed by conclusions in Sect. 6.

2 Wind farm modeling and optimization methodology

125 This section details the rotor modeling, wake modeling, wake superposition method, and analytical gradient computation method utilized in the study. The control strategy definitions, encompassing *no control*, *yaw control*, induction control (hereon referred to as *thrust control*), and joint yaw-induction control (hereon referred to as *joint control*), are formally defined. The optimization method employs dual number auto-differentiation for accurate and efficient optimization.



2.1 Rotor modeling

130 In this section, we introduce the engineering rotor modeling used in this study. The rotor can be modeled in an idealized manner using momentum theory based on the actuator disk model. This actuator disk modeling is introduced in Sect. 2.1.1, leveraging the Unified Momentum Model (Liew et al., 2024a) as the momentum model. Alternatively, the rotor can be modeled in a more realistic manner, using blade element momentum modeling. By coupling a blade element model with the Unified Momentum Model (Liew et al., 2024a), we achieve predictions for arbitrary thrust coefficients and yaw misalignment angles while also
 135 accounting for losses, blade pitch control, and tip speed ratio (generator torque) control, as described in Sect. 2.1.2. Both of these rotor models are naturally coupled with far-wake models that are introduced in Sect. 2.2.

2.1.1 Actuator disk momentum model

The first type of rotor modeling used in this investigation is an actuator disk model based on the Unified Momentum Model (Liew et al., 2024a), which extends the yawed actuator disk model developed by Heck et al. (2023). This model captures the
 140 behavior of a uniformly loaded actuator disk across operating regimes, including under yaw misalignment and high thrust conditions. Derived from first principles, the Unified Momentum Model describes rotor behavior in high thrust conditions without requiring empirical corrections like the Glauert correction (Glauert, 1926). This is achieved by relaxing the assumption used in classical momentum theory that the pressure far downstream of the actuator disk returns to ambient pressure. The model is represented by a system of five coupled equations with inputs for rotor yaw misalignment, γ , and modified thrust coefficient,
 145 C'_T . The Unified Momentum Model solves for rotor-normal axial induction, a_n , streamwise outlet velocity, u_4 , lateral outlet velocity, v_4 , near wake length, x_0 , and the pressure difference between far upstream and downstream of the streamtube, $p_4 - p_1$, as given by

$$a_n = 1 - \sqrt{\frac{u_\infty^2 - u_4^2 - v_4^2}{C'_T \cos^2(\gamma) u_\infty^2} - \frac{(p_4 - p_1)}{\frac{1}{2} \rho C'_T \cos^2(\gamma) u_\infty^2}} \quad (1)$$

$$u_4 = -\frac{1}{4} C'_T (1 - a_n) \cos^2(\gamma) u_\infty + \frac{u_\infty}{2} + \frac{1}{2} \sqrt{\left(\frac{1}{2} C'_T (1 - a_n) \cos^2(\gamma) u_\infty - u_\infty\right)^2 - \frac{4(p_4 - p_1)}{\rho}} \quad (2)$$

$$150 \quad v_4 = -\frac{1}{4} C'_T (1 - a_n)^2 \sin(\gamma) \cos^2(\gamma) u_\infty \quad (3)$$

$$\frac{x_0}{D} = \frac{\cos(\gamma)}{2\beta} \frac{u_\infty + u_4}{|u_\infty - u_4|} \sqrt{\frac{(1 - a_n) \cos(\gamma) u_\infty}{u_\infty + u_4}} \quad (4)$$

$$p_4 - p_1 = -\frac{1}{2\pi} \rho C'_T (1 - a_n)^2 \cos^2(\gamma) u_\infty^2 \arctan\left[\frac{1}{2} \frac{D}{x_0}\right] + p^{NL}(C'_T, \gamma, a_n, x_0), \quad (5)$$

where ρ is the air density, u_∞ is the ambient wind speed, D is the actuator disk diameter, $\beta = 0.1403$ is the shear layer growth rate parameter, and p^{NL} is the nonlinear pressure contribution term. Further details to this model can be found in Liew
 155 et al. (2024a). The shear layer growth parameter β is held fixed at the value described by Liew et al. (2024a) that agrees well with LES and is similar to the value used by Bastankhah and Porté-Agel (2016) and classical turbulent shear layer references therein. Note that the thrust input, C'_T is defined as $C'_T = 2\|\mathbf{F}_T\|/(\rho A_d u_d^2)$, where \mathbf{F}_T is the thrust force vector exerted by



the actuator disk, $A_d = \pi D^2/4$ is the disk area, and u_d is the wind velocity at the actuator disk which has been modified by induction. This is different from the more commonly used C_T , which is normalized using the freestream velocity, u_∞ . Using C'_T is advantageous due to its independence from the yaw angle γ , unlike the standard thrust coefficient C_T , which varies with yaw, as is discussed in more detail in Heck et al. (2023); Liew et al. (2024a). Importantly, an identically equivalent formulation of Eqs.(1)–(5) can be written based on the standard thrust coefficient C_T (Liew et al., 2024a). To make the Unified Momentum Model more straightforwardly compatible with blade element momentum modeling, an additional sixth equation is added to the system of equations to allow the more commonly used C_T to be used as an input to the model:

$$C'_T = \frac{C_T}{(1 - a_n)^2 \cos^2(\gamma)}, \quad (6)$$

where the thrust coefficient is defined $C_T \equiv 2\|\mathbf{F}_T\|/(\rho A_d u_\infty^2)$.

2.1.2 Blade element rotor model

The Unified Momentum Model presented above can be considered as the yawed analog to classical momentum theory commonly used in blade element momentum models. The Unified Momentum Model is also naturally extensible to high thrust and induction values, thus eliminating the need for empirical high thrust corrections that are commonly used in BEM. We can therefore formulate a blade element momentum (BEM) approach using the Unified Momentum Model in place of classical momentum theory, which accounts for the impact of yaw misalignment and high thrust coefficients on rotor induction from first principles. For simplicity, we match the Unified Momentum Model with the BEM model for rotor-average quantities of axial induction, \bar{a}_n , thrust coefficient, C'_T , initial streamwise wake velocity, u_4 , and initial lateral wake velocity, v_4 . The coupling between the Unified Momentum Model and blade element modeling at the sector or annulus level, commonly employed with BEM based on classical momentum theory, is also straightforward but will not be the focus of the present study.

The presented BEM model is formulated in non-dimensional radial units, $\mu = r/R$, where $R = D/2$ is the rotor radius and r is the radial coordinate. The inputs to the BEM model are the control set points for the yaw angle γ , blade pitch angle θ_p , and tip speed ratio, $\lambda = \Omega R/u_\infty$, where Ω is the rotor angular velocity. The turbine model is parameterized by blade solidity $\sigma_r(\mu)$, blade twist angle, $\theta_t(\mu)$, and airfoil lift and drag curves $C_l(\mu, \alpha)$, and $C_d(\mu, \alpha)$, which are a function of radial position and angle of attack, α . The BEM method is solved on a polar grid of (μ, ψ) , where ψ is the azimuthal position, and the local freestream non-dimensional wind speed at each of these points is $w(\mu, \psi)$. The following algorithm is iterated until convergence on the axial and tangential inductions, a_n and a' . First, an initial guess is made for the rotor-averaged induction:

$$a_n(\mu, \psi) = \bar{a}_n. \quad (7)$$

The wind speed vectors for axial and tangential velocity, assuming negligible tilt, are:

$$v_x(\mu, \psi) = U(\mu, \psi)(1 - a_n) \cos(\gamma) \quad (8)$$

$$v_t(\mu, \psi) = (1 + a')\lambda\mu - U(\mu, \psi)(1 - a_n) \cos(\psi) \sin(\gamma). \quad (9)$$



Note that this formulation can facilitate heterogeneous inflow (e.g. shear), however, in this study, uniform inflow ($U(\mu, \psi) = U_\infty$) is considered. The inflow speed and angle, w and ϕ , can be determined from v_x and v_t following

$$190 \quad w(\mu, \psi)^2 = v_x(\mu, \psi)^2 + v_t(\mu, \psi)^2 \quad (10)$$

$$\phi(\mu, \psi) = \tan^{-1} \left(\frac{v_x(\mu, \psi)}{v_t(\mu, \psi)} \right). \quad (11)$$

The angle of attack for each position on the polar grid is computed from the inflow angle, blade twist, and blade pitch angle:

$$\alpha(\mu, \psi) = \phi(\mu, \psi) - \theta_t(\mu) - \theta_p, \quad (12)$$

and the rotor normal and tangential force coefficients are

$$195 \quad C_n(\mu, \psi) = \cos(\phi)C_l(\mu, \alpha(\mu, \psi)) + \sin(\phi)C_d(\mu, \alpha(\mu, \psi)) \quad (13)$$

$$C_{\tan}(\mu, \psi) = \sin(\phi)C_l(\mu, \alpha(\mu, \psi)) - \cos(\phi)C_d(\mu, \alpha(\mu, \psi)). \quad (14)$$

Finally, the thrust coefficient, C_T , according to blade element modeling is calculated using:

$$C_T(\mu, \psi) = w(\mu, \psi)^2 \sigma(\mu) C_n(\mu, \psi). \quad (15)$$

200 $C_T(\mu, \psi)$ can now be integrated over the polar grid to arrive at the rotor-averaged thrust coefficient \bar{C}_T based on blade element modeling:

$$\bar{C}_T = \frac{1}{\pi} \int_0^1 \int_0^{2\pi} \mu C_T(\mu, \psi) d\psi d\mu. \quad (16)$$

We can now connect blade element modeling with momentum theory through the calculated thrust coefficient by using it as an input into the Unified Momentum Model to retrieve the rotor-normal axial induction and initial wake velocities:

$$[\bar{a}_n, \bar{u}_4, \bar{v}_4] = f_{\text{Unified}}(\bar{C}_T, \gamma), \quad (17)$$

205 where $f_{\text{Unified}}(C_T, \gamma)$ is the solution to the Unified Momentum Model using C_T as an input as described in Equations (1)–(6). The rotor-averaged rotor-normal axial induction, \bar{a}_n is retained to continue the fixed-point iteration loop for the BEM method and the rotor-averaged outlet velocities \bar{u}_4, \bar{v}_4 are retained for use as boundary conditions for the turbulent, far-wake deficit and wake deflection model, which is described in §2.2.

Next, the new induction profile is calculated such that its integral equals \bar{a}_n :

$$210 \quad a_n(\mu, \psi) = \bar{a}_n \frac{F(\mu)}{2 \int_0^1 \mu F(\mu) d\mu}, \quad (18)$$

where $F(\mu)$ is the tip loss function (Branlard, 2017, chapter 10),

$$F(\mu) = \frac{2}{\pi} \arccos \left(\exp \left(-\frac{N(1-\mu)}{2\mu \sin \phi} \right) \right). \quad (19)$$



Tangential induction is calculated similarly with

$$a'(\mu) = \frac{\sigma(\mu)}{4\mu^2(1 - a_n(\mu)) \cos \gamma} \frac{1}{2\pi} \int_0^{2\pi} w(\mu, \psi)^2 C_{\tan}^{\text{mod}}(\mu, \psi) d\psi, \quad (20)$$

215 where $C_{\tan}^{\text{mod}}(\mu, \psi) = C_{\tan}/F(\mu)$ is the tip loss corrected tangential force coefficient. Equations (8)–(17), are iterated using relaxation until the rotor-averaged, rotor-normal induction converges. The rotor-averaged power coefficient can then be calculated by integrating the local power coefficient over the rotor area

$$\bar{C}_p = \frac{1}{\pi} \int_0^1 \int_0^{2\pi} \lambda \mu^2 \sigma(\mu) w(\mu, \psi)^2 C_{\tan}(\mu, \psi) d\psi d\mu. \quad (21)$$

220 Again, the streamwise and lateral outlet velocities, which are used as inputs to the wake model, are calculated using the rotor-averaged thrust coefficient \bar{C}_T into the Unified Momentum Model Eqs. (2) and (3).

2.1.3 Turbine control surface

With the BEM method formulated, the control surface of a single turbine in uniform inflow can be calculated. The control surface describes how the coefficient of power, C_P , and the coefficient of thrust, C_T , vary with the blade pitch angle, θ_p , the rotor tip speed ratio, λ , and for the purposes of this study, the yaw misalignment of the rotor, γ . These surfaces, shown in
225 Fig. 1 for the IEA 15 MW reference wind turbine (Gaertner et al., 2020), are helpful in visualizing the optimal set points. As described in Liew et al. (2024b), the control surface distorts in yaw-misaligned cases, causing the C_p -maximizing pitch angle and tip speed ratio to vary as a function of yaw angle, usually shifting to lower pitch angles and tip speed ratios. Additionally, the thrust-minimizing trajectory, which is indicated as a curve across this surface, also shifts. The thrust-minimizing derating strategy has been shown to be the most effective derating strategy in terms of mitigating power losses due to wake interactions
230 (Vitulli et al., 2019; Pedersen and Larsen, 2020; Liew et al., 2024b). In the results to follow in Sect. 4.2.2, the thrust-minimizing trajectory will appear naturally as a result of the control optimization process.

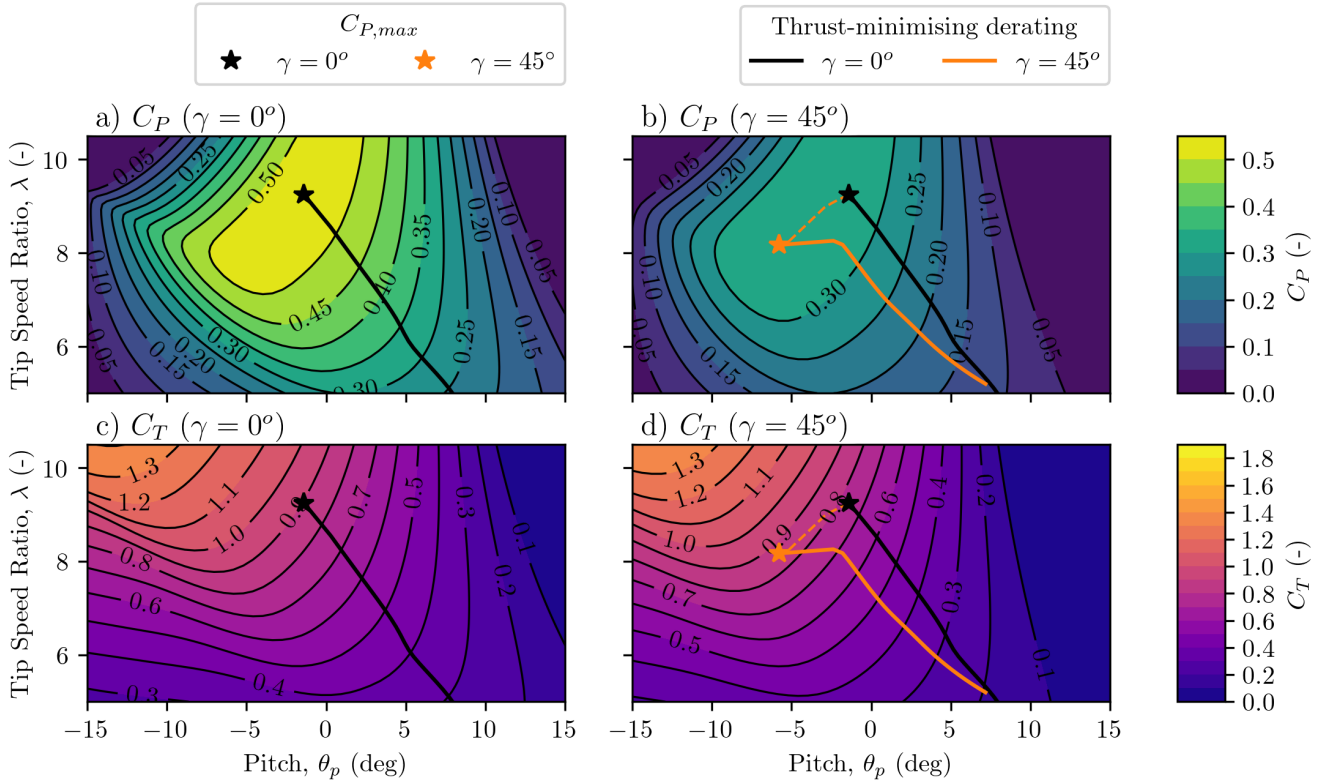


Figure 1. Contour plots of (a, b) power coefficient, C_P , and (c, d) thrust coefficient, C_T , as a function of blade pitch angle and rotor tip speed ratio for (a, c) a yaw aligned rotor and (b, d) a rotor yaw-misaligned by $\gamma = 45^\circ$. Minimum thrust derating trajectories are overlaid.

2.2 Wind farm modeling

To assess the interactions of turbines in a wind farm through different control strategies, the rotor model introduced in Sect. 2.1 is used for each wind turbine in an N -turbine wind farm as initial conditions for N wakes. The rotor model can use either the actuator disk model described in Sect. 2.1.1, or the blade element model described in Sect. 2.1.2. The steady-state wake model used in this study, described in detail in this section, is characterized by the following attributes: a wake deficit profile, a wake-added turbulence profile, wake deflection, and wake superposition. The static wind farm model that is developed as part of this investigation, known as MITWindfarm, is available open-source Liew et al. (2025).

The wakes are modeled using a steady-state Gaussian far-wake model (Bastankhah and Porté-Agel, 2014; Shapiro et al., 2018). Instead of adopting a fixed wake-spreading wake parameter, k_w , we instead use a variable formulation as a function of rotor effective turbulence intensity, TI . Specifically, we use the relation $k_w = a \cdot TI + b$ (Stevens et al., 2015; Niayifar and Porté-Agel, 2016), where a and b are set to 0.636 and 0, respectively, as explained in Sect. 4.2.3 by calibrating the wind farm model to LES wind farm power data. Note that the specific value of the proportionality constant a multiplied against TI differs from that used by Niayifar and Porté-Agel (2016), for example, because k_w differs from k^* (Howland et al., 2022a) and also because we



245 calibrate to LES in this study. For all wakes, an initial wake width of $\sigma_0 = D/\sqrt{8}$ is used (Bastankhah and Porté-Agel, 2016). The turbulence intensity considers both the wake-added turbulence intensity ΔTI , which is computed from the model proposed by Crespo and Hernández (1996), and the freestream ambient turbulence TI_{amb} such that $TI^2 = \Delta TI^2 + TI_{amb}^2$. When wakes are in superposition, only the largest value of ΔTI is used to compute the local TI . Other turbulence superposition methods could be investigated in future work (Delvaux et al., 2024; Klemmer and Howland, 2024).

250 The wake velocity deficit function $\delta u(x)$ is modeled as a smoothed step function in the vicinity of the rotor, and the lateral velocity is modeled similarly:

$$\frac{\delta u(x)}{u_r} = \frac{1 - (u_4/u_r)}{d_w^2(x)} \frac{1}{2} \left[1 + \operatorname{erf} \left(\frac{x}{\sqrt{2}D/2} \right) \right]; \quad \frac{\delta v(x)}{u_r} = \frac{-v_4/u_r}{d_w^2(x)} \frac{1}{2} \left[1 + \operatorname{erf} \left(\frac{x}{\sqrt{2}D/2} \right) \right], \quad (22)$$

where u_4 and v_4 are initial wake velocities from the rotor model, based on the Unified Momentum Model (Liew et al., 2024a), described in Sect. 2.1.1 and Sect. 2.1.2, and u_r is the velocity incident to the wake-generating rotor considering upstream turbine wakes. The normalized wake width, d_w is modeled as $d_w = 1 + k_w \log(1 + \exp(2(x - x_0)/D))$, where $x_0 = 1$ is the near-wake length (Shapiro et al., 2018; Howland et al., 2022b). Finally, the wake deflection distance, y_c , is computed by numerically integrating $\delta v(x)$ from Eq. (22) in the x -direction such that

$$y_c(x) = \int_0^x \frac{-\delta v(x')}{u_r} dx'. \quad (23)$$

In this work, we use the Gaussian wake model proposed by Shapiro et al. (2018). Beginning with the linearized Reynolds-Averaged Navier–Stokes equations, they proposed a model for the wake deficit field of an individual turbine:

$$\Delta u(x, y, z) = \delta u(x - x_t) \frac{D^2}{8\sigma_0^2} \exp \left(-\frac{(y - y_t - y_c(x))^2 + (z - z_t - z_h)^2}{2\sigma_0^2(x - x_t)d_w^2(x - x_t)} \right). \quad (24)$$

where the location (x, y, z) is defined in the global coordinate system, (x_t, y_t, z_t) is the location of the turbine generating the wake in the global coordinate system, and the freestream velocity is in the positive x -direction.

To model the effect of wakes from multiple upstream turbines, we use the wake superposition method proposed by Niayifar and Porté-Agel (2016)

$$u(x, y, z) = u^B(x, y, z) - \sum_{i \in x_i < x} \Delta u_i(x, y, z), \quad (25)$$

where u is the streamwise velocity at location (x, y, z) in the global coordinate system, u_B is the streamwise velocity excluding all wake effects, $\Delta u_i(x, y, z)$ is the wake deficit at the location of interest caused by turbine i given by Eq. (24), and the sum is taken over all turbines upstream of the location of interest. This superposition method yields similar predictions in most settings (Howland et al., 2020b) to the momentum conserving superposition method developed by Zong and Porté-Agel (2020).

2.3 Controller methodologies and optimization problems

In this study, we define and compare four control methodologies. To define the control set points of an entire wind farm, we define two vectors of control variables for the actuator disk (AD) model, $C'_T = [C'_{T,1}, \dots, C'_{T,N}]^T$ and $\gamma = [\gamma_1, \dots, \gamma_N]^T$.



Likewise, three vectors are defined for the BEM model: $\theta_p = [\theta_{p,1}, \dots, \theta_{p,N}]^T$, $\lambda = [\lambda_1, \dots, \lambda_N]^T$, and $\gamma = [\gamma_1, \dots, \gamma_N]^T$. The following four control strategies can therefore be defined as different combinations of fixed and free control variables. For the control variables that are fixed for a given control strategy, the value of that set point is chosen as the single-turbine optimal. We define the following single-turbine optimal set points as $C'_{T,opt} = 2$ and $\gamma_{opt} = 0^\circ$ for the actuator disk model, corresponding to the classical Betz limit ($C_{T,opt} = 8/9$). For the BEM model, the optimal set points are $\theta_{p,opt} = -1.132^\circ$, $\lambda_{opt} = 9.138$ and $\gamma_{opt} = 0^\circ$, where the values for $\theta_{p,opt}$ and λ_{opt} are determined using the BEM model described in Sect. 2.1.2 using the IEA 15 MW reference wind turbine model (Gaertner et al., 2020) for uniform, zero turbulence inflow.

The first methodology, referred to as the *no control* case, involves standard greedy wind turbine control where all control variables are set to their unwaked optimum values. The second methodology, *thrust control*, allows for changes in rotor thrust while maintaining turbine yaw alignment. In the context of the actuator disk rotor model, *thrust control* is achieved by varying C'_T while keeping $\gamma = 0^\circ$. *Thrust control* is implemented differently using the BEM rotor model as thrust cannot be directly set. Rather, tip speed ratio λ and blade pitch angle θ_p are controlled while fixing $\gamma = 0^\circ$. The third methodology, *yaw control*, enables the optimization of the turbine's yaw angle while keeping pitch angle and tip speed ratio (or C'_T in the case of the actuator disk) fixed at their unwaked optimal values. The fourth methodology, *joint control*, involves the optimization of all control variables. The optimization problem can be generalized as:

$$\text{minimize} \quad -C_{P,\text{farm}}(\theta_p, \lambda, \gamma) \tag{26}$$

$$\text{with respect to} \quad \text{free variables} \tag{27}$$

$$\text{subject to} \quad \text{fixed variables} \tag{28}$$

where the free and fixed variables for each strategy are indicated in Table 1.

Table 1. The definition of the control methods and variables. The optimal values for the fixed variables are set to the single-turbine optimal set points. For the AD rotor, $C'_{T,opt} = 2.0$ (corresponding to $C_{T,opt} = 8/9$), and for the BEM rotor, $\theta_{p,opt} = -1.132^\circ$, and $\lambda_{opt} = 9.138$. Both rotors use $\gamma_{opt} = 0^\circ$.

Control Method	Free Variables		Fixed Variables	
	AD	BEM	AD	BEM
No Control	-	-	C'_T, γ	$\theta_p, \lambda, \gamma$
Thrust Control	C'_T	θ_p, λ	γ	γ
Yaw Control	γ	γ	C'_T	θ_p, λ
Joint Control	C'_T, γ	$\theta_p, \lambda, \gamma$	-	-



2.4 Dual number approach to auto-differentiation

To perform efficient optimization, we leverage automatic differentiation to compute analytical derivatives. Forward mode
295 autodifferentiation using dual numbers is employed in this study to efficiently compute gradients during the optimization
process (Bücker, 2006; Baydin et al., 2018). A dual number is defined as:

$$z = a + b\epsilon, \quad (29)$$

where $a, b \in \mathbb{R}$ are the primal and dual parts of z , respectively, and ϵ is the dual unit, where $\epsilon^2 = 0$. To see how dual numbers
are used in automatic differentiation, we evaluate a real-valued analytic function f with a dual number argument:

$$300 \quad f(a + b\epsilon) = \sum_{n=0}^{\infty} \frac{f^{(n)}(a)b^n\epsilon^n}{n!} = f(a) + bf'(a)\epsilon. \quad (30)$$

The dual part of the result is equal to the derivative of the function evaluated at the primal part a , scaled by the dual part b . In the
context of optimization, the availability of exact gradients concerning the optimization variables enables precise computation
of the Jacobian matrix. This, in turn, facilitates the utilization of gradient-based optimization algorithms. The above definition,
which is valid for scalar functions, can be extended to vector functions and to multiple dual units, which is equivalent to
305 assigning multiple variables for which we compute gradients. A further generalization of the dual part, which can be extended
to an array of arbitrary dimensions, carries both the values of the vector function and the corresponding directional derivatives,
providing a convenient way to compute gradients in the context of array operations and optimization involving multivariate
functions.

We implement dual number-based automatic differentiation in Python using operation overloading and monkey patching.
310 This unobtrusively overrides all pertinent NumPy and SciPy operations within the wind farm model from Sect. 2. As a result,
no modifications are necessary in the wind farm model code to enable efficient and straightforward analytical calculations of
gradients for wind farm flow control optimization. The primal and dual components for the input variables and all intermedi-
ate computations are organized into separate arrays, allowing for efficient, vectorized, machine-code operations in numerical
programming packages such as NumPy. The motivation for this formulation is threefold: exact gradients can be computed on
315 any variable of choice, vectorized operations are efficiently computed on arbitrary-sized input arrays through broadcasting, and
finally, gradients can be computed without having to modify the underlying forward model code.

Automatic differentiation, largely popularized by machine learning software libraries, has been integrated into engineering
wind farm models such as PyWake (Pedersen et al., 2023), which utilizes the Autograd package (Maclaurin et al., 2015) for
efficient and flexible autodifferentiation. The majority of studies exploring automatic differentiation for wind farm design and
320 control have been in wind farm layout optimization (c.f. Guirguis et al., 2016; Quick et al., 2023; Valotta Rodrigues et al.,
2024). In this study, the input variables for which gradients are computed correspond with wind farm control parameters, but
the same framework can be used for other optimization problems, for example, computing gradients with respect to the turbine
coordinates to study wind farm layout optimization.

3 Large eddy simulation setup

325 Large eddy simulations (LES) of a wind farm in a conventionally neutral atmospheric boundary layer (ABL) are used to compare with the fast-running wind farm modeling presented in §2. We perform LES using the open-source, pseudo-spectral code PadéOps (numerical details given in Howland et al. (2020b); Heck and Howland (2025)). A finite wind farm is simulated using the concurrent-precursor method (Stevens et al., 2014), where a fringe region (Nordström et al., 1999) in the primary domain is used to replenish the momentum deficit in the wake region. The precursor simulation, which uses synchronized
 330 time-stepping with the primary simulation, does not contain turbines and uses periodic boundary conditions in the horizontal directions. The primary and precursor simulation use the same domain size, which is given in Table 2 along with other LES parameters. Note that the 25-turbine wind farm domain is substantially larger than the 2-turbine layout to mitigate the effect of the domain size on the results.

The wind farm is modeled using the actuator disk approach (Calaf et al., 2010). Turbines impart a force on the flow $F_T =$
 335 $\frac{1}{2}\rho\pi R^2 u_d^2 C'_T$, where u_d is the velocity at the disk and C'_T is the local thrust coefficient. We use the correction factor introduced by Shapiro et al. (2019a) to correct the disk velocity u_d from the Gaussian filtering of the actuator disk. The wind farm is rotated in the LES domain to achieve different incident wind angles. Control set points C'_T and γ for each wind turbine are prescribed as an input and do not vary in time because the conventionally neutral boundary layer is quasi-stationary after the startup transience (Allaerts and Meyers, 2015). The turbine diameter D is set to 100 m, and the turbine hub height is $z_h = 100$ m.

340 The atmospheric boundary layer is initialized using the procedure from Liu et al. (2021). The surface is modeled with a Monin-Obukhov wall model using a surface roughness $z_0 = 1$ mm in all simulations. Conventionally neutral conditions are imposed using a zero heat flux condition at the surface. A frame angle controller (Sescu and Meneveau, 2014) is used after the turbulent ABL reaches a quasi-steady state, which aligns the flow at hub height with the x -direction. The frame angle controller is turned off before the concurrent-precursor simulations are initialized, and wind farm statistics are averaged until
 345 power and wake statistics converge, given by T_{avg} in Table 2. Time-averaging begins after two flow-through times ($2L_x/G$) to allow transient effects to decay and the wind farm wake to fully develop. A comparison of the differences between the wind farm LES parameters is given in Table 2.

Table 2. LES simulation parameters. Both simulations use a surface roughness $z_0 = 1$ mm, turbine diameter $D = 100$ m, hub height $z_h = 100$ m, reference potential temperature $\theta_0 = 300$ K, and Coriolis parameter $f_c = 10^{-4} \text{ s}^{-1}$.

Variable	2-turbine layout	25-turbine layout
Grid resolution (m)	(10, 5, 5)	(24, 12, 6)
Domain size (km)	(3.84, 1.28, 1.28)	(18.4, 9.2, 1.5)
G (m s^{-1})	8	10
U_{hub} (m s^{-1})	7.2	8.7
TI_{hub} (-)	5.5%	5.6%
Γ (K km^{-1})	1	3
T_{avg} (hr)	2	4



4 Results

In this section, we present the results of the control-optimized wind farm model evaluations. Optimizations using actuator disk and BEM rotor models are compared, and a selection of cases are compared to LES data. Four controller strategies are compared: *no control*, *thrust control*, *yaw control*, and *joint control*. We begin with the two-turbine results in Sect. 4.1. We first highlight the optimal actuator disk and BEM set points in the modeling framework for a sweep of wind directions. Here, we compare the optimal wind farm control between predictions from the gradient-based optimization of the fast-running wind farm model and from a parametric sweep over different control set points in LES. Following the two-turbine results, the 5×5 wind farm array is presented in Sect. 4.2. Again, we first focus on the wake model, exploring a full wind rose of wind directions and turbine spacing distances to investigate the impact of wind farm control on farm power and thrust. Then, we select one wind direction to compare the wind farm modeling framework against LES of a 5×5 wind farm layout to evaluate both the model accuracy and the implications of the different control strategies in LES. Unless otherwise stated, the results presented below are from the engineering wind farm model presented in Sect. 2.

4.1 Two-turbine system

The two-turbine system, visualized in Fig. 2, serves as a representative example that highlights the key characteristics of wake interactions between turbines, offering insights into how various wind farm control strategies perform in a larger wind farm setting. The two-turbine case is modeled using the fast-running wind farm model over a range of wind directions using both the AD and BEM rotor models. At each wind direction, the four different control strategies are optimized to maximize the collective power output of the two-turbine system. Additionally, in §4.1.2, one wind direction (3.8°) is simulated using LES with a brute force sweep over C'_T and γ to find the thrust and yaw set points that maximize the combined power of the two wind turbines in LES, and to compare these values with the optimal values predicted by the engineering model.

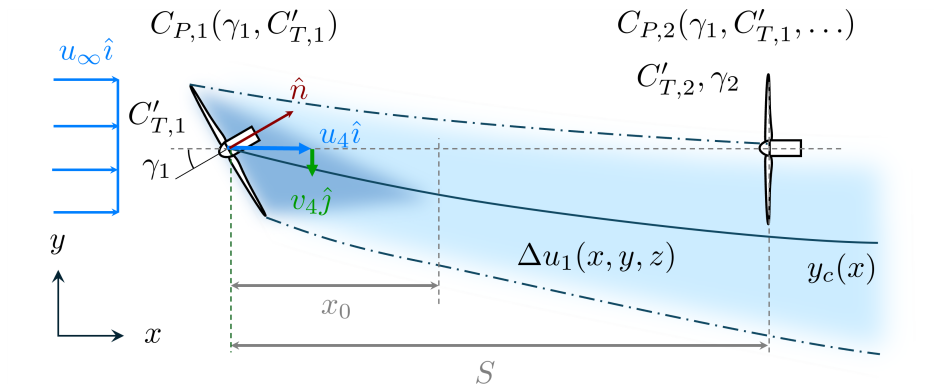


Figure 2. Schematic of the two-turbine wind farm showing the wind farm layout, AD control variables, and rotor and wake model outputs in full-wake conditions ($\alpha_{wd} = 0^\circ$). The leading turbine (1) is controlled while the downstream turbine (2) is kept at the Betz optimal control set point ($C'_{T,2} = 2, \gamma_2 = 0$).



4.1.1 Two-turbine engineering wind farm model optimal results

The two-turbine case investigated here is defined with a turbine separation distance S , shown in Fig. 2. We sweep over wind directions α_{wd} to change the layout of the wind farm, where $\alpha_{\text{wd}} = 0^\circ$ results in a full-wake scenario. A change in wind direction is applied by rotating the wind turbine coordinates such that the trailing turbine is located $S \cos(\alpha_{\text{wd}})$ downstream with a lateral offset distance of $S \sin(\alpha_{\text{wd}})$ from the leading turbine. That is, positive wind directions favor positive yaw misalignment angles. In the results below, we will also evaluate the dependence on the inter-turbine separation distance S . In all cases, the turbulence intensity is set to $TI = 5.5\%$.

Model-optimal results for a turbine spacing of $S = 6D$ for the AD and BEM model are shown in Fig. 3. For wind directions where wake interactions decrease power production downwind (i.e., $\alpha_{\text{wd}} \pm 15^\circ$), the model predicts an increase in collective power production through flow control, as shown in Fig. 3(a). *Yaw control* outperforms *thrust control* to increase collective power production, except in a narrow window encompassing full-wake conditions around a wind direction of zero degrees. In contrast, the optimal *joint control* strategy performs a combination of *yaw control* and *thrust control* for most wind directions, except around the full-wake scenario where a smooth transition to *thrust control* is observed. In particular, *joint control* surpasses *yaw control* in full-wake conditions and *thrust control* in partial-wake conditions. As a result, *joint control* requires derating over a narrower range of wind directions compared to *thrust control* alone and exceeds or matches the performance of *yaw control* for all wind directions. This finding underscores the efficacy of integrated *yaw* and *thrust control* strategies in optimizing turbine performance. Additionally, both the AD and BEM models demonstrate that *joint control* necessitates an increase in the thrust coefficient (C'_T) for partial wake conditions, highlighting the coupled nature of *yaw control* with induction/thrust. We note that the thrust coefficient C_T , which is normalized to the freestream wind speed u_∞^2 instead of the projected freestream wind speed $u_\infty^2 \cos^2(\gamma)$, decreases under *yaw* and *joint control* because the momentum flux available to the turbine decreases with $\cos^2(\gamma)$ as the turbine is yaw misaligned (c.f. Bastankhah and Porté-Agel, 2016). Power losses due to yaw-misalignment of the upstream turbine are mitigated through compensatory increases in turbine thrust (Heck et al., 2023), and the increase in thrust also deflects the wake further away from the downwind turbine (Heck et al., 2024).

Moving to the BEM optimal control (dashed lines in Fig. 3), the trends between control strategies in maximizing wind farm power $C_{P,\text{farm}}$ echo the AD rotor model. *Joint control* outperforms *yaw control* and *thrust control* at all wind directions, and transitions to purely *thrust control* in full-wake conditions for this wind farm layout. Comparing the BEM and AD rotor models, there are several primary discrepancies. First, the overall farm power and leading turbine thrust C_T are lower in the BEM model than for the AD turbine model due to root and tip losses and other aerodynamic inefficiencies. Second, in the *yaw control* BEM optimizations, the blade pitch and TSR are fixed at their power-maximizing values for a freestanding, yaw-aligned turbine (Table 1). However, the resulting thrust coefficient (C_T or C'_T) deviates from the Betz-optimal value when the turbine is yaw-misaligned, as shown in Fig. 3(c-d). This highlights that for a turbine with realistic control parameters (γ , θ_p , λ), prescribing *yaw control* also modifies the thrust in general, resulting in a combination of *yaw* and *thrust control* that is fundamental to yaw misaligning the wind turbine while holding pitch and TSR fixed. Rather than suboptimally relying on the standard turbine control when yawing in the *joint control* strategy, we leverage the interconnected nature of turbine thrust and

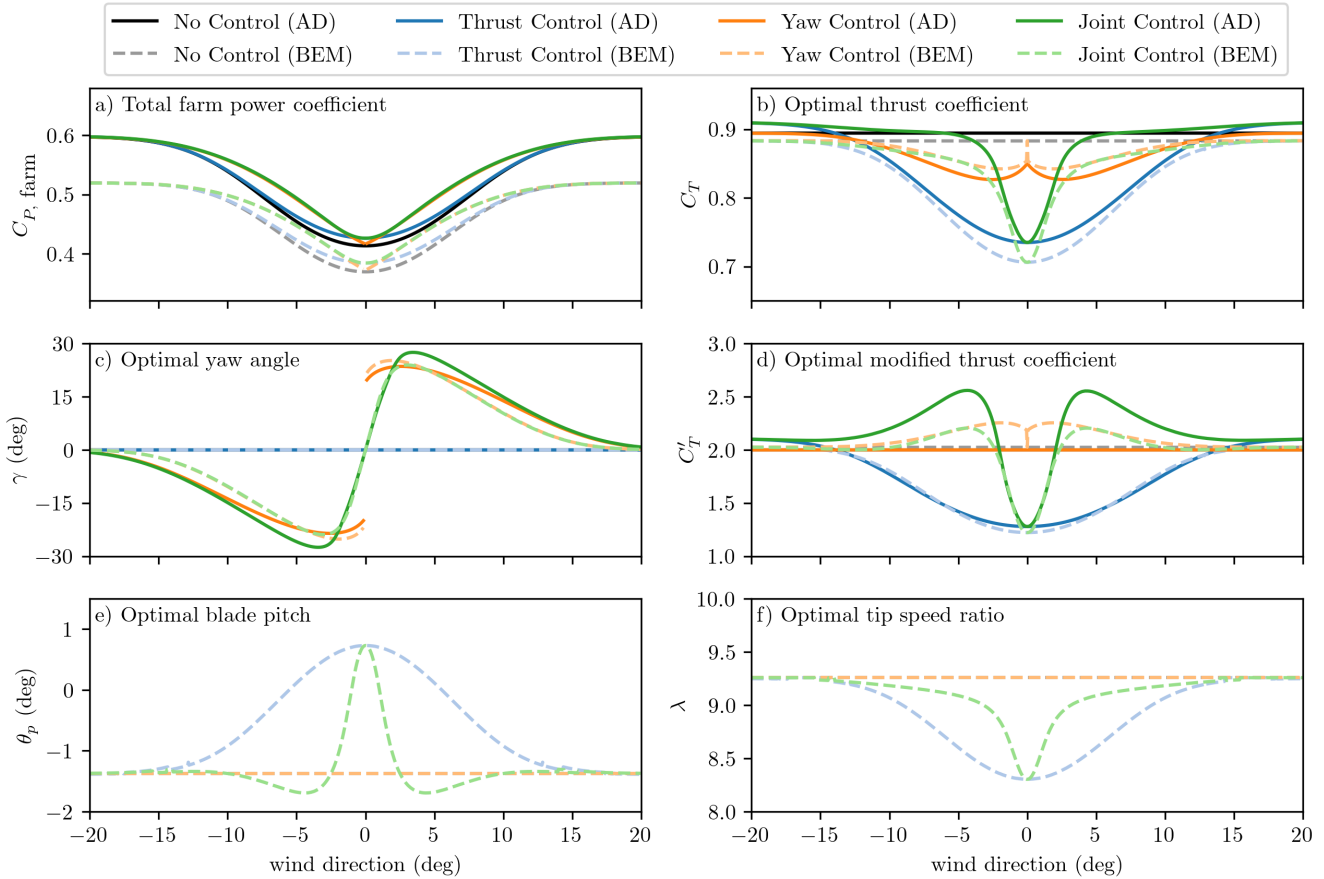


Figure 3. Control-optimized results for the two-turbine system ($S = 6D$ turbine spacing) over a range of wind directions. Four control methods (*no control*, *thrust control*, *yaw control* and *joint control*) and two rotor models (actuator disk, solid lines, and blade element momentum, dashed lines) are compared.

yaw to intentionally manipulate the blade pitch and TSR concurrently with yaw angle. To achieve the necessary derating for joint control, the BEM results indicated that pitch increases by approximately 2 degrees, while TSR decreases by about 1 based on the specific turbine arrangement under consideration. Finally, the resulting modified thrust coefficient C'_T is lower for the BEM rotor than the AD rotor under *joint control*. Although the BEM model can achieve the same modified thrust coefficient as the AD model, doing so requires a reduced pitch angle, as shown in Fig. 3(d-e), which significantly lowers the rotor torque and therefore the rotor power. Therefore, under *joint control*, the BEM model optimal thrust coefficient is persistently lower than the AD model for each wind direction, and the yaw set point is also reduced to mitigate power loss from the leading turbine.

A final added benefit of *joint control* is a smooth yaw set point, as shown in Fig. 3(c), which does not occur for *yaw control*. A discontinuity in optimal yaw angle as a function of wind direction, which occurs because the wake impinging on the downstream turbine switches from one side to the other, is highlighted by the wind farm model at a turbine spacing of



6D. The yaw angle discontinuity under *yaw control* is present in both AD and BEM control optimizations. In contrast, *joint control* transitions seamlessly between *yaw control* and *thrust control* across a wind direction of zero, and the discontinuity in the yaw set point when using *yaw control* alone vanishes. This denotes an additional potential benefit in using *joint control* as it can remove the ambiguous optimal control set point in a full wake scenario, which is present in *yaw control*, and allows for a continuous gradient-based solution to the optimal control set point, which is often difficult when using yaw steering alone due to this discontinuity. However, the smooth transition in yaw angle set point under *joint control* is not universal. Specifically, the yaw set point is smooth as long as *thrust control* is the optimal control strategy in full-wake conditions. This occurs at tighter turbine spacings and when ambient turbulence intensity is sufficiently large. By increasing the turbine spacing distance to $10D$ of the two-turbine wind farm, the smooth transition in joint control for the leading turbine yaw set point vanishes, as shown in Fig. 4. We emphasize that although *joint control* is not guaranteed to produce a smooth and continuous yaw set point, *joint control* nevertheless mitigates discontinuities in many relevant operating conditions. The primary benefit of *joint control* predicted by the engineering wind farm model is the enhanced power extraction across all wind directions, compared to *yaw*, *thrust*, and *no control* strategies.

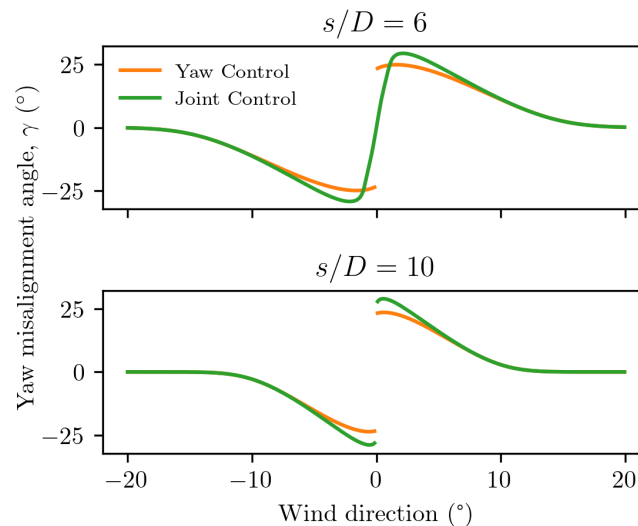


Figure 4. Optimal yaw set points for the two-turbine wind farm, similar to Figure 3(c), except with $10D$ spacing and AD only for *yaw control* and *joint control* strategies.

425 In summary, the two-turbine wind farm provides a valuable case study of the benefits of *joint yaw-induction control* for wind farm power optimization. At a turbine spacing distance of $6D$, the *joint control* strategy smoothly transitions from *yaw control* to *thrust control* in full-wake conditions to maximize collective power extraction. Additionally, the *joint control* strategy combines *yaw control* with increases in thrust C'_T to enhance power extraction in partial-wake conditions. The optimal set points are also presented using blade pitch angle, tip speed ratio, and yaw angle by coupling the momentum model with a
430 blade element model, indicating that derating is achieved through a combination of increasing the blade pitch angle as well as



decreasing the tip speed ratio. Using the *joint control* strategy, optimal BEM set points increase C'_T in partial wake conditions primarily through a negative blade pitch angle. The mechanisms for increasing collective wind farm power in the two-turbine wind farm are instructive for parsing the model predictions in the larger 5×5 wind turbine array.

4.1.2 Two-turbine LES comparison

435 To evaluate different wind turbine control strategies using LES, we study a two-turbine wind turbine array with an inter-turbine spacing of $S = 6D$. An incident wind angle of 3.8° from being fully aligned with the wind turbine rows is selected for all LES runs, creating a partial wake scenario with a lateral wind turbine spacing of $0.4D$. For each independent two-turbine simulation, the layout (i.e. wind direction and spacing) is fixed, and the leading turbine thrust coefficient C'_T and yaw γ set points are prescribed to a value that does not vary in time. Positive yaw misalignments are favored in this partial wake
440 scenario (see Fig. 2), and as such, we only simulate $\gamma \geq 0^\circ$. The waked turbine is set to the power-maximizing Betz limit of $(C'_{T,2}, \gamma_2) = (2.0, 0^\circ)$ while the leading turbine yaw set point is varied such that $\gamma_1 \in [0^\circ, 45^\circ]$. The leading turbine thrust is also swept over a parameter range of $C'_T \in [0.4, 4.4]$, totaling 210 independent large eddy simulation cases. Power statistics are time-averaged for two hours after initial transients decay. We evaluate different control strategies by analyzing subsets of the control parameter sweep in LES constrained to the fixed and free variables in Table 1; the *no control* baseline is the LES run
445 $C'_T = 2.0, \gamma = 0^\circ$.

First, we examine the LES results before comparing them with model predictions. Contours of the total farm efficiency $C_{P, farm} = \frac{1}{N} \sum C_{P,i}$, leading turbine power $C_{P,1}$, and waked turbine power $C_{P,2}$ are shown in Fig. 5. As efficiency is defined as $C_{P,i} = P_i / (\frac{1}{2} \rho A_d u_\infty^3)$, which is normalized by the freestream velocity u_∞ , farm efficiency is simply a re-normalization of wind farm power. Therefore, maximizing wind farm efficiency is analogous to maximizing wind farm power. In Fig. 5(a),
450 contours of wind farm efficiency from LES are shown, where each white point represents an individual LES case. The farm power-maximizing turbine set points for the leading turbine are $(C'_{T,1}, \gamma_1) = (4.0, 25^\circ)$, as marked by the blue star on all subfigures. The farm power-maximizing operation of the leading turbine does not maximize its own power, which occurs at the Betz optimal $C'_T = 2.0$ and zero yaw misalignment. Importantly, the power-maximizing set point of the leading turbine is realized at a combination of yaw misalignment and changes in rotor thrust. Specifically, the array power maximizing thrust
455 coefficient is overinductive when yaw misalignment is imposed on the leading turbine. That is, for this wind farm configuration, joint control enables additional power extraction by the wind farm in LES compared to *yaw control* or *thrust control* alone. Power production using the optimal set points results in 21% increased power production relative to the *no control* case. In comparison with *joint control*, the LES-optimal power gain under *yaw control* and *thrust control* is 18% and 1.5%, respectively.

Interestingly, the gain in $C_{P, farm}$ under *joint control* is larger than the individual gains from *yaw control* and *thrust control*
460 added together, demonstrating a nonlinear and synergistic interaction between *thrust* and *yaw control* that leads to further gains from flow control. We parse the mechanisms for power increase under *joint control* and explain the large leading turbine thrust coefficient in three ways. First, the leading turbine mitigates its own power loss due to yaw misalignment with compensatory increases in thrust (Heck et al., 2023; Liew et al., 2024a). This is because the turbine induction factor is a function of yaw misalignment as well as thrust coefficient. As the turbine yaws, maintaining $C'_T = C'_{T, Betz} / \cos^2(\gamma)$ maximizes $C_{P,1}$ by in-



465 creasing the induction to make up for the reduction of thrust due to yaw misalignment. Second, the wake of the leading turbine
 is altered by its control strategy (Cossu, 2021; Heck et al., 2024). Namely, as thrust increases, wake recovery and mixing
 are enhanced by the increasing shear magnitude between the wake velocity, which decreases with increasing thrust, and the
 surrounding flow. Therefore, wakes of high-thrust turbines recover faster than wakes at low thrust coefficients (Annoni et al.,
 2016; Martínez-Tossas et al., 2022). Third, when the leading turbine is yaw-misaligned, increasing the thrust leads to increased
 470 wake deflection and curling around the downwind turbine (Howland et al., 2016; Bastankhah and Porté-Agel, 2016), mitigating
 wake interactions and increasing downwind power output (Cossu, 2021). For these three reasons, the optimal control strategy
 in LES is a combination of yaw misalignment and an increase in leading turbine thrust.

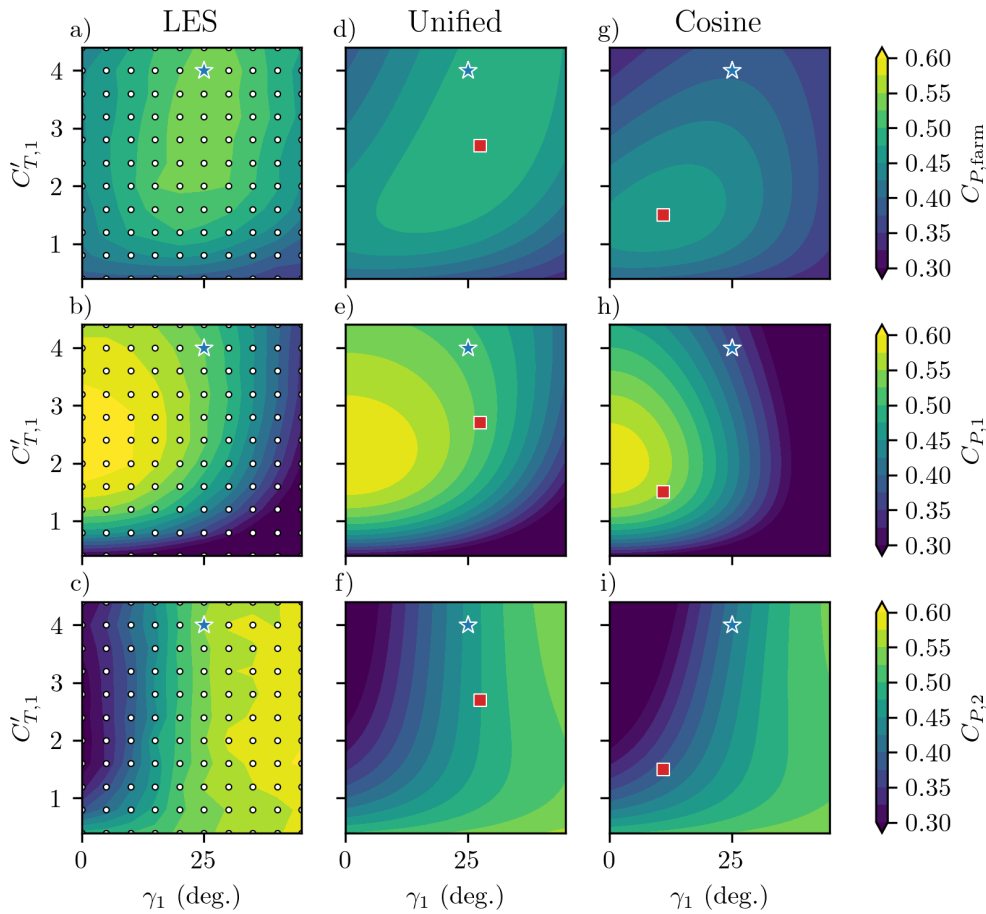


Figure 5. LES wind turbine power for a two-turbine wind farm at a wind angle of 3.8° . White dots represent individual LES simulations. The LES $C_{P,farm}$ -maximizing set point is shown in all subfigures with the blue star, while the wake model $C_{P,farm}$ -maximizing set point is shown with the red square.



Next, we use the wind farm model presented in §2 to model the same two-turbine configuration. In this section, to evaluate the dependence of the engineering model results on different rotor submodels, the Gaussian wake model (Bastankhah and Porté-
475 Agel, 2014; Shapiro et al., 2018) is coupled with the initial conditions from different momentum models to predict the farm power-maximizing set points. The Gaussian wake model depends on a wake spreading rate $k_w = 0.636 \cdot TI$, $\sigma_0 = D/\sqrt{8}$, and $x_0 = 1D$, where TI is the rotor-equivalent turbulence intensity. These are the wake model parameters found in the calibration as described in Sect. 4.2. In the Gaussian wake model, the initial streamwise and lateral velocities u_4 and v_4 are taken from the momentum model, Eqs. 2 and 3, respectively. To compare the effectiveness of wind farm control with various modeling
480 decisions, we show two momentum closures to compute the axial induction factor and near-wake velocities. First, we use the Unified Momentum Model (Liew et al., 2024a) to compute the axial induction factor a_n from the rotor set points γ and C'_T . Turbine power is computed $P = \frac{1}{2} \rho A_d u_d^3 C'_T$, where the velocity at the disk u_d is modified by induction, as well as by upstream turbine wakes. Second, as a baseline method, we use a cosine power-yaw model which is based on an assumption that the axial induction a_n does not change with yaw misalignment angle, and the relationship between thrust and induction is computed
485 using one-dimensional momentum theory (Burton et al., 2011). This means that $P \propto P(\gamma = 0) \cos^3(\gamma)$, where $P(\gamma = 0)$ is the turbine power in yaw aligned operation.

Model-predicted set point predictions which maximize $C_{P,\text{farm}}$ in the wake model are shown by the red squares in Fig. 5(d-i). The power-maximizing set point for the upstream turbine predicted by the Unified model is $\gamma = 28^\circ$ and $C'_T = 2.7$. In this wind farm configuration, the wake model predicts increasing thrust to increase the wake deflection from the downstream turbine,
490 and to mitigate the power lost due to yaw misalignment from the leading turbine (Heck et al., 2024). Interpolating the LES data at the wake model-predicted set point results in a 19.2% increase in power relative to the *no control* case. Recall that the global optimum from the brute force sweep over different parameters in LES is 21% power gain. Therefore, the wind farm model based on the Unified Momentum Model results in 1.8% less power gain than the true power-maximizing control set point.

By contrast, the cosine model predicts optimal set points at a more modest yaw misalignment in combination with turbine
495 derating. Coupled with the same Gaussian far wake model, the cosine model-predicted power-maximizing set point results in a yaw of $\gamma = 11^\circ$ combined with slight derating, $C'_T = 1.5$. Interpolating this model set point in LES results in a power gain of only 9.5%. We note that if we empirically approximate $P(\gamma) \approx P(\gamma = 0) \cos^{p_P}(\gamma)$ (Medici, 2005; Gebraad et al., 2016) with $p_P = 1.9$ calibrated from LES data at $C'_T = 2$, the qualitative results are unaffected, and the model-predicted power-maximizing set point occurs at $C'_T = 1.6$, $\gamma = 17.4^\circ$. Because the cosine models ignore any dependence of yaw on turbine
500 induction, the benefits of operating at higher rotor thrust are not captured. Using the Unified Momentum Model that captures the physical relationship between induction, yaw, and power realizes more accurate model-optimal set points and leads to more effective wind farm control.

The results in Fig. 5 indicate that although wind farm modeling based on the Unified Momentum Model improves predictions for the combined power of the two-turbine array, there are still substantial discrepancies relative to the LES data. Examining
505 $C_{P,1}$ in Fig. 5(b, e, h), we can see that the Unified Momentum Model is able to reliably predict the magnitude and the shape of the dependence of $C_{P,1}$ on thrust and yaw, while the cosine model yields larger errors for $C_{P,1}$ at larger values of both the yaw angle and the thrust coefficient. On the other hand, both rotor models share a far-wake model, and larger discrepancies



between the LES data and model predictions for $C_{P,2}$ are present for both the Unified rotor model and the cosine-based rotor model, particularly with increasing yaw angle magnitude γ_1 .

510 To summarize our findings for the two-turbine wind farm, we observe the critical importance of utilizing rotor models that capture the synergistic, nonlinear, and interactive relationship between yaw misalignment and rotor induction. The cosine model, which cannot encode any dependence of yawed power loss on the thrust coefficient, predicts operating set points that significantly underperform when compared with the physics-based Unified Momentum Model. Specifically, the realized power gain from the cosine model is 9.5%, while the realized power gain from the Unified model is 19.2%. However, both rotor models
515 use an axisymmetric Gaussian wake, where the wake spreading rate and near-wake length do not depend on the turbine control set point. As a result, the benefits of the downstream power gain from the leading turbine operation are underestimated. Control optimization using more advanced wake modeling methods that capture the three-dimensional wake structure (Martínez-Tossas et al., 2021; Bastankhah et al., 2022; Narasimhan et al., 2022, 2024) and models that capture feedback between the wake-added turbulence and the wake recovery (Pedersen et al., 2022; Risco et al., 2023; Klemmer and Howland, 2024) are important to
520 further improve wind farm flow model predictions.

4.2 Wind farm flow control in a 25 turbine wind farm

In our investigation of the broader implications of joint yaw-induction control, we turn our attention to a larger wind farm configuration, specifically a diamond layout comprising 25 turbines. The study of the four presented control strategies in this layout provides a representative example of how such control strategies operate in more realistic multi-turbine wind farms. The
525 wind farm layout is depicted in Fig. 6.

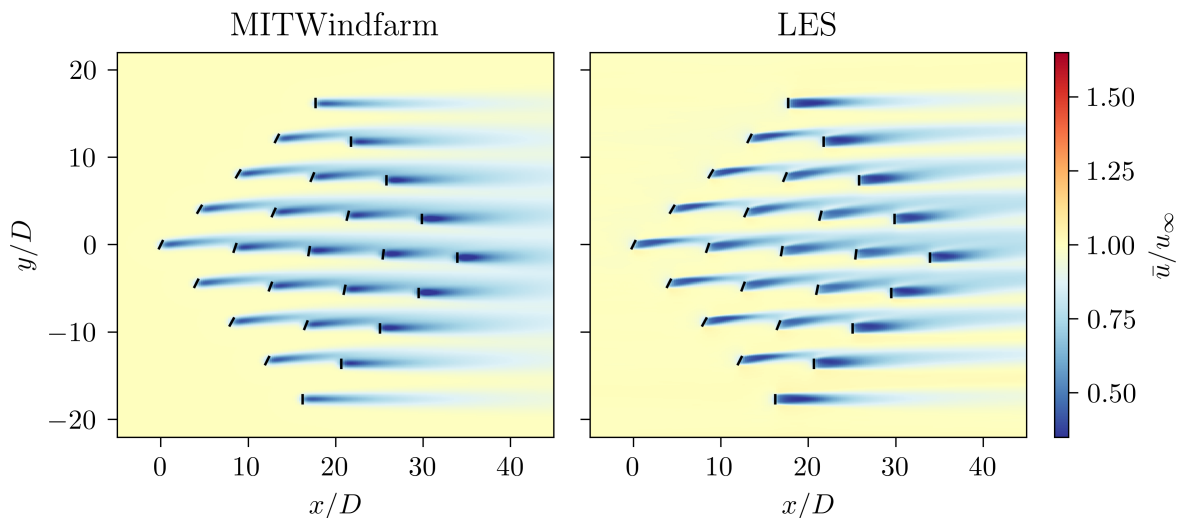


Figure 6. Layout of the large wind farm with a diamond arrangement operating under *joint control*, comparing the wind farm flow model MITWindfarm and time-averaged large eddy simulation flow fields.



The wind farm control set points are optimized using the four target control strategies outlined in Sect. 2.3 to maximize wind farm power. Using the wind farm modeling framework, we evaluate a full revolution of wind directions in 0.05° intervals. Leveraging the four-way rotational symmetry inherent in the wind farm layout, we only need to evaluate a quarter of the wind rose to capture a full range of wind directions (Van Der Laan et al., 2022). Both the blade element momentum (BEM) and actuator disk (AD) rotor models are employed in our wind farm model evaluations. We vary the turbine spacing distance between $2D$ and $10D$ using the AD rotor model to assess the impact of turbine spacing on the efficacy of wind farm flow control using the wind farm model. Wind farm model evaluations utilizing the BEM turbine rotor model are conducted exclusively at a $6D$ turbine spacing. Alongside the wind farm model evaluations, LES are conducted using the actuator disk model for selected wind directions to validate certain results, as elaborated in Sect. 3. As in the two-turbine results section, the presented results are generated using the fast-running wind farm model, rather than LES, unless stated otherwise.

4.2.1 Effect of turbine spacing on wind farm control performance

To investigate the dependence of wind farm control strategy on turbine spacing, we vary the spacing in the 5×5 -turbine square wind farm layout. For each wind direction, the optimization algorithm identifies the power-maximizing wind turbine set points subject to the constraints of the control strategy (see Table 1). We compare the average farm power, aggregated uniformly over all wind directions, to a baseline case that uses greedy individual turbine control (*no control*).

As shown in Fig. 7, the wind farm model predicts increases in farm energy production for all control strategies, with the greatest benefits from wind farm control at tighter turbine spacing distances and diminishing effectiveness at larger spacings. Across all spacings, *joint control* consistently outperforms *yaw control* and *thrust control*, particularly in the range of $3D$ to $6D$ of inter-turbine spacing. *Yaw control* surpasses *thrust control* in terms of power output for turbine spacing greater than $\sim 3.3D$. In subsequent analysis, we focus on a separation distance of $6D$, noting that the qualitative trends between control strategies are not strongly dependent on the turbine spacing distance for spacings larger than $\approx 4D$.

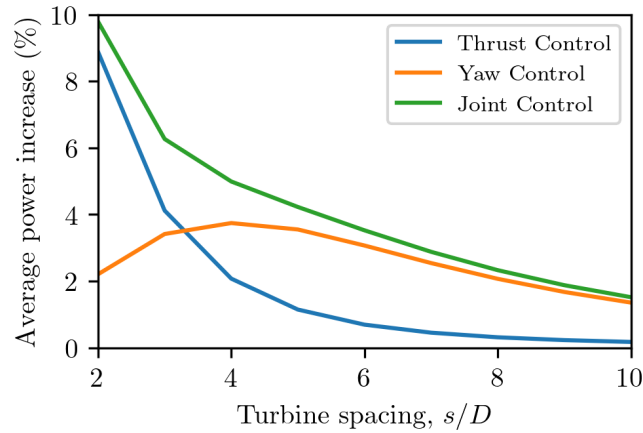


Figure 7. Wind farm power increase versus turbine spacing for the 5×5 wind farm configuration using optimal control setpoints for three control strategies (*thrust control*, *yaw control*, and *joint control*). Wind rose-averaged power increase is aggregated uniformly over all wind directions and normalized by the *no control* strategy. Varying spacing distances are evaluated and optimized using the AD rotor in the wind farm model.

4.2.2 Individual turbine performance

Shifting focus from the farm-aggregated power, we now focus on the performance and BEM optimal set points for individual turbine in the wind farm. The wind farm layout exhibits symmetry, resulting in six unique turbines after accounting for mirror and rotational symmetries. These turbines are labeled from *A* to *F* as defined in Fig. 8, where *A* is the most exterior turbine group and *F* is the most interior turbine group.

The power rose in Fig. 8 shows $C_{P,\text{farm}} = \sum P_i / (\frac{1}{2} \rho A_d u_\infty^3 N)$, where $N = 25$ is the number of wind turbines in the farm and P_i is the average power production of turbine i , as a function of wind direction for a given control strategy. The largest power losses occur at wind directions $\alpha_{\text{wd}} = 0^\circ$ and $\alpha_{\text{wd}} = 45^\circ$, when the incident is aligned along the diagonals and the rows of the wind farm, respectively. In these scenarios, wind farm control has the greatest potential to increase farm power relative to a baseline without wind farm control. Therefore, the largest deviations from individually optimal turbine set points generally occur around 0° or 45° , as well as 90° offsets of these angles following the symmetries of the wind farm.

Turbine set points as a function of incident wind direction for the *joint control* case are shown in Fig. 8 for the BEM rotor model. Exterior turbines (e.g. turbine *A*) generally exhibit less pronounced control action compared to interior counterparts (e.g. turbine *F*). When the wind direction is fully aligned along the rows or diagonals, the thrust set point decreases below the individual optimum. This indicates that in full-wake conditions, the *joint control* strategy is performing *thrust control* to derate leading turbines, similar to the two-turbine wind farm scenario. In partial wake conditions, the optimal yaw set point shows the greatest degree of yaw misalignment. In these situations, the optimal modified thrust coefficient, C'_T , increases for the leading row turbines. This mirrors the behavior in the two-turbine scenario, where C'_T is increased for the leading row turbines to increase wake deflection from downwind turbines, as well as to mitigate power loss due to yaw misalignment. A major benefit



of the *joint control* is that it can smoothly transition between these strategies, performing both turbine derating when no yaw misalignment is enforced and increasing the local thrust coefficient when yaw misalignment is present.

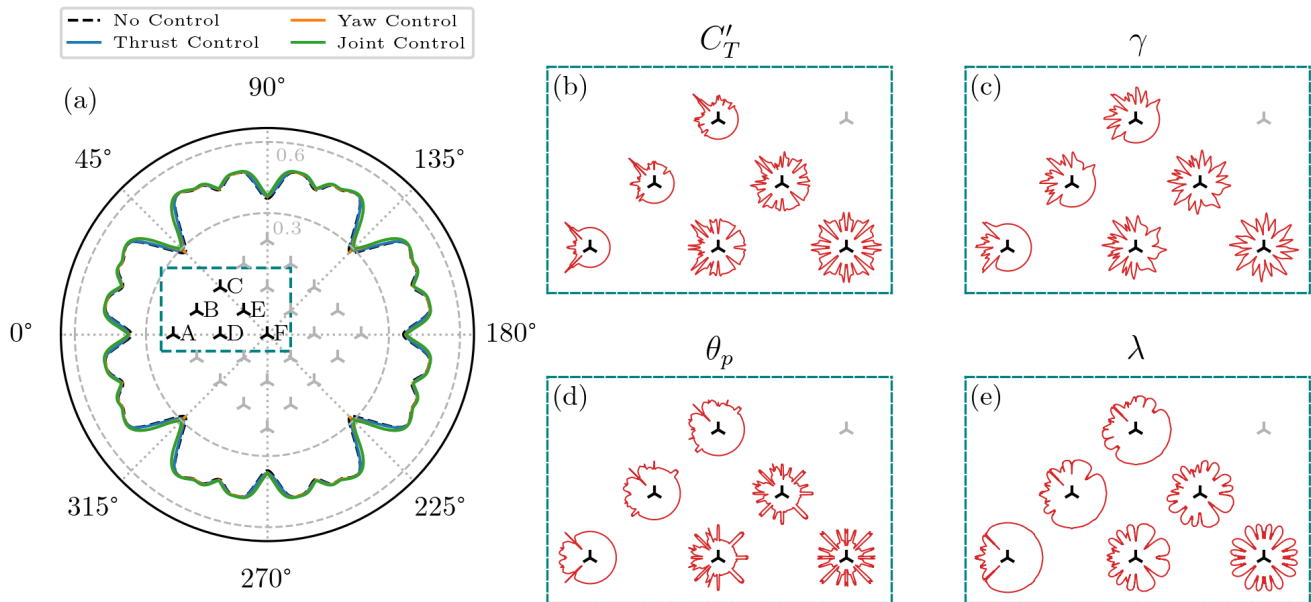


Figure 8. (a) Wind farm power roses for the four wind farm control strategies evaluated with the BEM rotor in the engineering wind farm model. Rotational and mirror symmetry turbine groups are labeled. (right) optimal turbine control set point roses for *joint control* for the 6 symmetric turbine groups of the wind farm. Set point roses shown: (b) modified thrust coefficient C'_T , (c) yaw angle γ , (d) blade pitch angle θ_p , (e) and tip speed ratio λ .

For the BEM model turbine, derating during full wake conditions is accomplished with a combination of increasing the blade pitch θ_p as well as decreasing the tip speed ratio λ . The optimal operating strategy tends to follow the minimum thrust trajectory for a given yaw angle as shown in Fig. 9, although variations may arise, particularly for downstream turbines due to wind field heterogeneity. The minimum thrust trajectory is not enforced here. Instead, the efficient gradient-based optimization of the BEM model, coupled with a wake model, generally tends to follow the expected minimum thrust trend. More generally, it could be challenging to tabulate a heuristic minimum thrust trajectory because it depends on the yaw misalignment and on the turbine model. Here, we rely on direct optimization of the physics-based model for each condition instead. When the turbine is yaw misaligned, the optimal pitch angle and tip speed ratio tend to decrease. This is a result of the changing shape of the pitch-TSR contour in yaw-misaligned conditions, described in detail in Liew et al. (2024b). Different yaw misalignment angles γ are shown with varying lightness in Fig. 9. When comparing the AD model to the BEM model turbine, the yaw set points are similar; however, the thrust set points (C'_T) in the BEM model are lower than those in the AD model (not shown). We observe the same trends in yaw and thrust when comparing the BEM to AD model in the two-turbine scenario, as shown in Fig. 3.

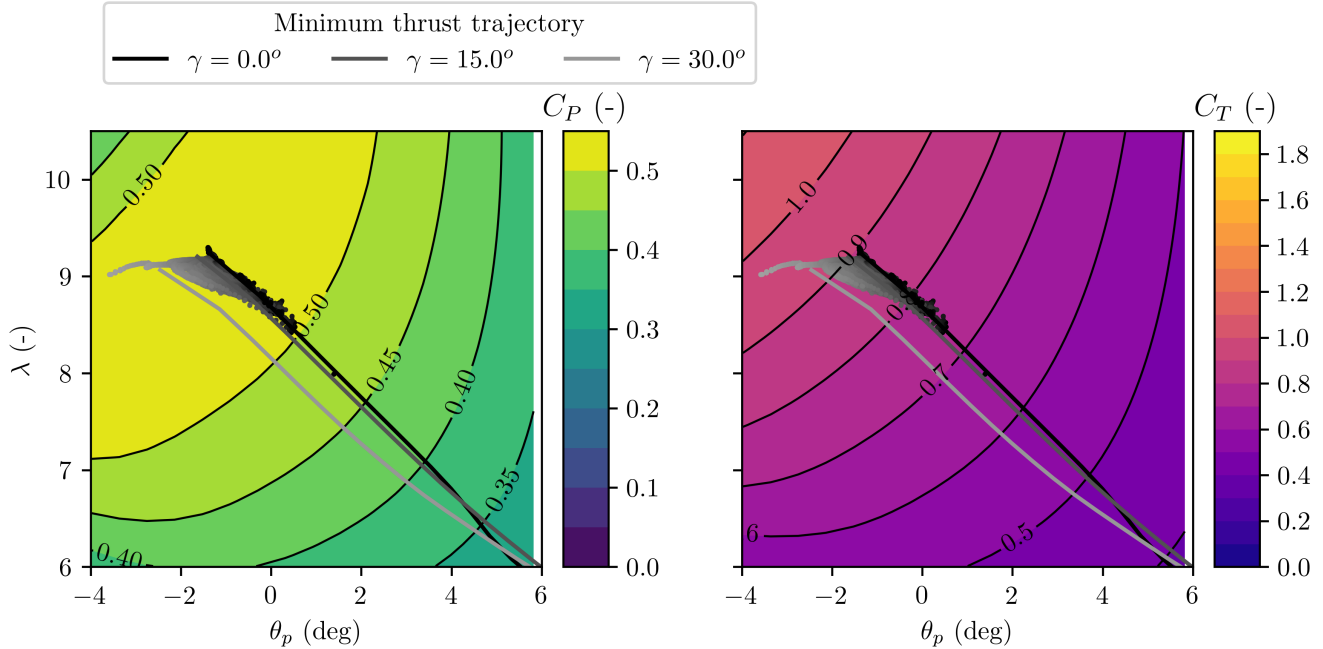


Figure 9. Optimal pitch angle and tip speed ratios from turbines in the 25-turbine wind farm ($6D$ spacing, with set points evaluated from all wind directions) presented on the control surface from Fig. 1 for a yaw-aligned freestream turbine. The lightness of the points indicates the associated yaw angle of the turbine. The thrust-minimizing control trajectories calculated in Sect. 2.1.3 are indicated as solid lines.

580 To calculate the change in average power and thrust across all wind directions, we again assume equal weighting for each direction. The turbine-level and wind farm-level power gains and change in thrust, compared to the *no control* strategy, are shown in Fig. 10. Interior turbines show the largest gain in wind rose-averaged power from performing collective wind farm flow control of any strategy. Furthermore, in all cases, *joint control* provides a larger power increase than *yaw control*, particularly for interior turbines. For example, group *F* turbines experience a 6.1% and 6.8% power increase over the *no control* case for *yaw control* and *joint control*, respectively. Conversely, the exterior turbine group *A* experiences a more marginal 0.2%
 585 power decrease and 0.1% power decrease over the *no control* case for *yaw* and *joint control*, respectively.

The wind rose-averaged turbine thrust level tends to increase for interior turbines when applying flow control. Here, the turbine thrust is again averaged over an equal distribution of all wind directions and normalized by the freestream wind speed ($C_T = T / (\frac{1}{2} \rho A_d u_\infty^2)$). Both *joint* and *yaw control* increase the average turbine thrust C_T over individual control due to decreased wake interactions and increased wind speeds in the interior of the farm. Similar to the farm-wide power coefficient, the farm-wide thrust coefficient is given by $C_{T, \text{farm}} = \sum T_i / (\frac{1}{2} \rho A_d u_\infty^2 N)$, where T_i is the average thrust of turbine i across all wind directions. *Yaw control* presents the highest level of thrust with a farm-wide average thrust level increase of 3.0%, compared to 0.8% for *joint control*. By contrast, *thrust control* has a net 4.2% decrease in farm-wide average thrust, which is approximately uniformly distributed across individual turbines in the wind farm. Thrust level is highly correlated with fatigue
 590



595 loading in turbines (Galinos et al., 2018), therefore it is possible that *thrust control* could reduce loads for all turbines in the
 farm. *Joint control*, while having an increase in thrust compared to the reference case, has a notably lower thrust level than
yaw control due to the lower optimal thrust coefficients in the BEM *joint control* set points around full-wake conditions, which
 are also shown in the two-turbine wind farm. While the aggregated change in farm-wide thrust will depend on the wind farm
 layout and site conditions, this case study indicates that *joint control* has potential benefits in power gains and with minimal
 600 thrust load increase. Future work can more formally express a multi-objective wind plant optimization considering power and
 loads (Van Dijk et al., 2017; Croce et al., 2024) or profit/lifetime aware control (Braunbehrens et al., 2024).

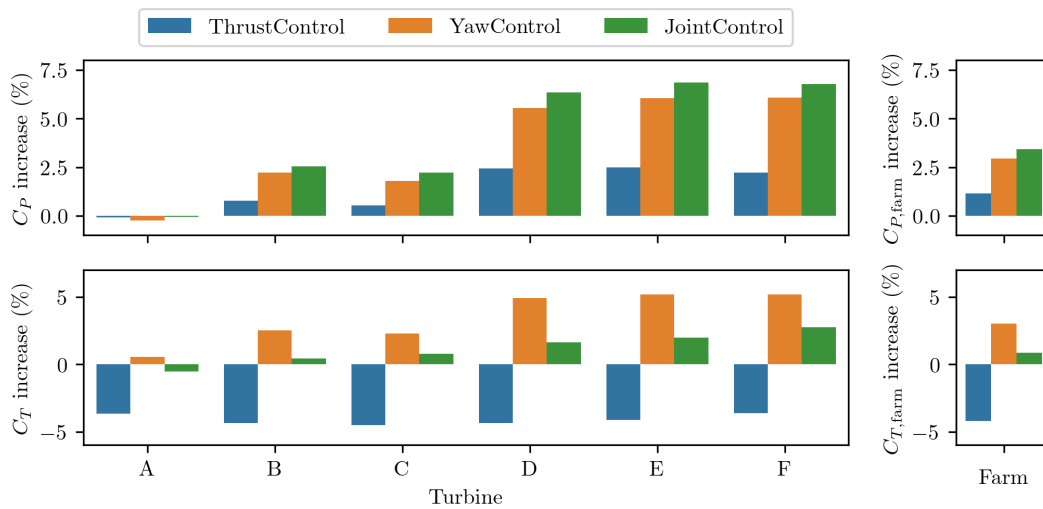


Figure 10. Optimal performance per symmetric turbine groups as well as the entire wind farm for *thrust control*, *yaw control* and *joint control* for the 5×5 wind farm configuration. Turbine symmetry groups are presented from most exterior (*A*) to most interior (*F*) positions in the wind farm. Power and thrust are aggregated uniformly over all wind directions and normalized by the *no control* strategy.

4.2.3 LES comparison

To evaluate the efficacy of the engineering wind farm model in its ability to increase wind farm power extraction through flow control, we conduct a comparative study of four control strategies on the 25-turbine wind farm layout using large eddy
 605 simulations (LES). A single wind direction of 2.5° is selected to be simulated in LES indicated in Fig. 11, which allows for near-maximal benefit from wind farm control as predicted by the wind farm flow model presented in Sect. 2.

The wind farm model is calibrated initially to a *no control* baseline simulation with all turbines operating at the Betz optimal thrust $C'_T = 2$ and zero yaw-misalignment. A simple model for the wake spreading rate $k_w = a \cdot TI + b$ is fit to the turbine-level power from the no control LES data. Although there is an anticipated dependence of k_w on thrust C'_T (Annoni et al., 2016;
 610 Heck et al., 2024), we do not include it in our calibration because all *no control* turbines operate at the same C'_T . Actuator disk-modeled turbines in LES tend to overpredict power production relative to momentum theory due to the regularization method



of the disk forcing (Shapiro et al., 2019a). Even with the correction factor from Shapiro et al. (2019b) applied, the power from the AD-modeled turbines in LES overshoots the Betz limit by approximately 4% at $C'_T = 2.0$. To avoid bias in the wake spreading calibration parameters from this persistent over-prediction in power, all LES power data is normalized to the power produced by the upstream-most turbine operating at the Betz limit in the *no control* case ($C_{P1,Betz} = 0.619$). Likewise, the wake model power output is normalized by the Betz limit ($C_{P,Betz} = 16/27$). The optimal fit minimizes the root-mean-square error of normalized turbine power between the LES and the wake model output from MITWindfarm, resulting in calibration parameters $a = 0.636$ and $b = 0$. Subsequently, we use the calibrated wind farm model in low-fidelity evaluations using the model presented in Sect. 2 (MITWindfarm) to determine the optimal set points for each control strategy. The model-optimal set points (C'_T, γ), which are provided in Appendix A, are then assigned to turbines in LES, and we use the high-fidelity simulation to evaluate the efficacy of different control strategies, as well as the accuracy of the farm wake model. Turbine set points do not change in time, and separate LES simulations are run for each control strategy. Each separate simulation receives identical initial conditions and boundary conditions, as well as the same concurrent precursor, to ensure the only differences arising in the LES cases result from the wind farm flow control method used.

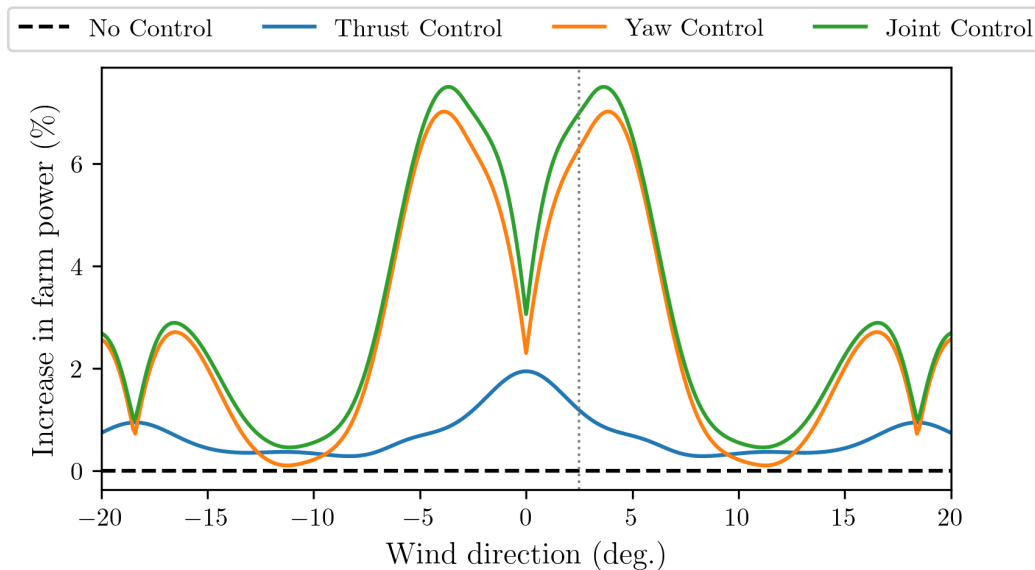


Figure 11. Gain in wind farm power $C_{P,farm}$ due to wind farm control, relative to a no control baseline and evaluated by the engineering wind farm model, for the 5×5 diamond wind farm across a range of wind directions using AD turbines. The gray vertical dotted line shows the selected wind direction ($\alpha_{wd} = 2.5^\circ$) for the LES cases.

We start by comparing time- and farm-averaged power $C_{P,farm}$ between LES and the wind farm model presented in §2. In Fig. 12, the change in LES farm-wide average power coefficient $C_{P,farm}$ is shown relative to a *no control* baseline. Two standard deviations of 10-minute-averaged $C_{P,farm}$ about the mean value are shown in the LES data to compare the change in power from wind farm control with variations in power due to atmospheric boundary layer turbulence (internal variability). Both



630 *joint control* and *yaw control* produce significantly more power than the *no control* baseline in both rotor models. In contrast, *thrust control* fails to statistically enhance power production, even leading to a slight drop (1.3%) in mean farm power that is not statistically significant. The primary cause of the net power loss under *thrust control* in LES is due to the dependence of the wake spreading rate k_w on the turbine thrust C'_T (or induction a), which is not considered here. Specifically, higher thrust coefficients lead to faster wake break down which partially mitigates the potential benefits of the lower initial wake deficit associated with lower thrust coefficients. The discrepancy in farm power prediction between the wind farm model and LES is similar to Annoni et al. (2016). This effect was also noted in the two-turbine wind farm in Sect. 4.1.2. As thrust decreases, the maximum wake velocity deficit (i.e., $u_\infty - u_4$) is reduced, which also reduces turbulent mixing, leading to slower wake recovery (Annoni et al., 2016; Heck et al., 2024).

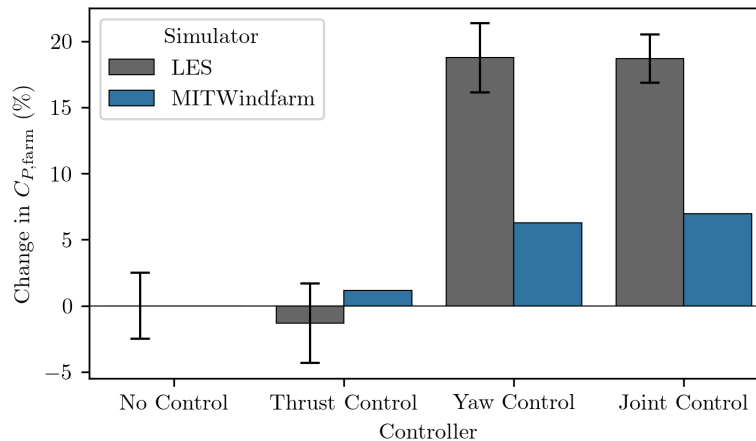


Figure 12. Wind farm power gain, relative to *no control*, in LES and the analytical model MITWindfarm for three flow control strategies. Error bars in the LES data represent two standard deviations of wind farm power over 10-minute averages.

When the turbine is permitted to yaw, as in *yaw control* and *joint control*, power gain from flow control is significant compared to *no control* or *thrust control*. In both *yaw* and *joint control* scenarios, increases in wind farm power exceed variations due to ABL turbulence on 10-minute time windows, resulting in 18.8% and 18.7% increases in $C_{P,\text{farm}}$, respectively. The difference in wind farm power output between *yaw control* and *joint control* is not statistically significant on a 95% confidence interval for the 4 hours of time averaging simulated (not shown). We highlight that the benefit of *yaw control* and *joint control* is approximately three times higher in the LES than in the wind farm model, which predicts power gains of only 6.3% and 7.0%, respectively. To understand this discrepancy, we examine the performance of the wake model at the turbine level.

645 Figure 13 shows the row-averaged turbine power simulated in LES and the engineering wind farm model for all control strategies. The row-averaged turbine power is normalized by most upstream turbine in the wind farm in the *no control* case, which operates at the Betz limit, to normalize any LES dependence on the turbine regularization methodology. Dashed error bars represent the minimum and maximum turbine power for that turbine row. In the *no control* set points, differences in power



650 production for the leading-row chevron of turbines are primarily due to local wind farm blockage effects (Nishino and Draper, 2015; Bleeg et al., 2018; Nygaard et al., 2020), which is also shown as turbine-level power data in Appendix A. In addition to blockage effects, columns of turbines operate differently as a function of the number of downstream turbines for the *thrust*, *yaw*, and *joint control* strategies.

The wind farm model is calibrated to the *no control* LES data. Therefore, the agreement in Fig. 13(a) is closer than the out-of-sample wind farm model power predictions under different control strategies. Power predictions from the engineering wind farm model for *thrust control* also yield relatively low error, shown in Fig. 13(b). The main discrepancy in the *thrust control* power predictions is an overestimation in the engineering model for the second row/chevron of turbines. Power is overestimated in the second-row *thrust control* turbines because the wake modeling framework does not consider the decreased wake spreading rate as thrust decreases, which is also observed in the two-turbine wind farm data. As a result, the second-row turbines produce less power in LES than predicted by the model, resulting in power loss under *thrust control* in LES compared with a *no control* baseline.

Power discrepancies between the wind farm model and LES are larger downwind of yawed turbines under *yaw control* and *joint control* strategies, shown in Fig. 13(c) and (d), respectively. For the leading row of wind turbines, power predictions of yaw-misaligned rotors are in good agreement with LES, with model errors less than the uncertainty. Similar to the two-turbine case, this further establishes confidence in the Unified Momentum Model for yaw misaligned rotors. However, the wind farm model persistently underpredicts the power produced by rotors downstream of yawed turbines because of the non-Gaussian, three-dimensional structure of the wind turbine wakes, which also causes underpredictions in the power of waked turbine in the two-turbine wind farm (see Fig. 5(c,f,i)). Because more waked turbines exist in the large wind farm than in the two-turbine wind farm, the error in farm power is compounded. Additional factors such as secondary steering and wake superposition likely further exacerbate errors in the wind farm modeled power.

670 In summary, the 5×5 turbine wind farm LES cases provide an encouraging outlook for wind farm flow control strategies to increase collective power production. Relative to a *no control* baseline, where all turbines operate at the Betz optimal $C_T' = 2$, $\gamma = 0$, turbine set points under *yaw* and *joint control* increase wind farm power by 18%. In contrast, farm power under *thrust control* decreased by 1.3%. Primary discrepancies in turbine-level power between LES and the wind farm model under the *thrust control* strategy are due to the dependence of wake spreading on the turbine thrust (induction factor). In *yaw control* and *joint control*, primary discrepancies in turbine-level power between LES and the wind farm model are due to the three-dimensional structure of the curled wake. As a result, the model-predicted power gain from *yaw control* or *joint control* is underestimated by roughly a factor of three. For all control strategies, model power predictions of the leading-row freestream turbines are in excellent agreement with LES, validating the Unified Momentum Model against the LES. However, *joint control* based on optimal set points from the engineering model presented in Sect. 2 fails to achieve larger gains than wake steering alone. This differs from the two-turbine case and is likely driven by the low accuracy of the engineering model used to model wakes of yaw-misaligned turbines for control applications. In other words, it may be possible that there is a global optimum control strategy for the 25 turbine wind farm that is a combination of yaw misalignment and thrust control, but the present fast-running model used in this study is not able to reliably identify this control strategy.

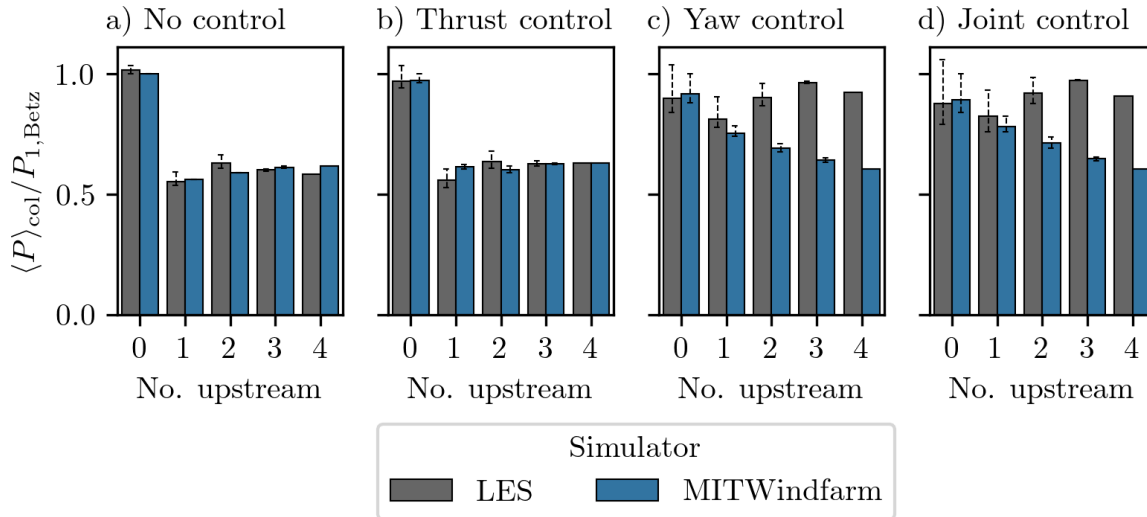


Figure 13. Column-averaged wind power P of individual turbines as a function of the number of upstream turbines for all control strategies. Power values are normalized by a freestream turbine operating at the Betz limit $P_{1, \text{Betz}}$ in each simulator (LES and MITWindfarm). Ranges indicate the maximum and minimum wind turbine power values in each column. Note that under wind farm flow control, turbines operate differently in each column due to the changing number of downstream turbines.

Integrating fast-running models that capture the three-dimensional curled structure of yawed wind turbine wakes (Howland et al., 2016; Bastankhah and Porté-Agel, 2016; Martínez-Tossas et al., 2021; Bastankhah et al., 2022; Narasimhan et al., 2022, 2024) into the gradient-based optimization methodology for wind farm control should be pursued in future work to reduce error in the wake modeling and ideally to improve the power production when employing model-based wind farm flow control. These wake models can be coupled to the Unified Momentum Model which provides generalized wake initial conditions across yaw angles and thrust coefficients.

690 5 Discussion

Model-based wind farm flow control requires accurate and computationally efficient predictions of the rotor and wake aerodynamics in the atmospheric boundary layer. The findings of this study are enabled by the physics-based Unified Momentum Model (Liew et al., 2024a) for rotor predictions relating turbine induction and power to thrust and yaw. In both the two-turbine wind farm (Fig. 5(b, e)) and in the 25-turbine wind farm (Fig. 13), predictions of power produced by the leading-row turbines show significantly better agreement with LES than power predictions of waked turbines. While there are deficiencies in the Unified approach, which neglects wind shear and turbulence in the aerodynamic modeling, the key relationships between thrust, yaw, and power exhibit good agreement across a wide range of thrust coefficients (up to $C'_T = 4.4$) and yaw misalignment angles (up to 45°). The Unified Momentum Model is compatible with autodifferentiation, enabling gradient-based optimiza-



tion for flow control. On the contrary, a primary deficiency in the wind farm flow modeling lies within the wake modeling
700 framework. In the two-turbine and 25-turbine wind farms, power predictions downstream of yawed turbines are consistently
underpredicted due to the limitations of the axisymmetric Gaussian wake model used here. However, it remains a technical
challenge for future work to utilize more advanced wake models (e.g. Martínez-Tossas et al., 2021; Bastankhah et al., 2022;
Narasimhan et al., 2022, 2024), which capture the structure and deflection of the curled wake, in gradient-based optimization.
An axisymmetric Gaussian wake model also degrades in accuracy in the near-wake, which affects flow control optimization
705 under tight turbine spacing distances (Schreiber et al., 2020; Blondel and Cathelain, 2020; Ali et al., 2024). Innovative solutions
to efficient and accurate wake modeling for yawed wind turbine wakes and small inter-turbine spacings in the context of wind
farm control optimization are needed to fully realize the benefits of wind farm flow control.

While *joint yaw-thrust control* offers significant advantages to yaw or *thrust control* alone, implementing a *joint control*
strategy in real-world scenarios presents several challenges. A primary obstacle is the need for highly accurate wind direction
710 estimates across the entire wind farm. This precision is crucial for assigning appropriate control setpoints to each turbine, as
these setpoints vary depending on whether a turbine experiences partial-wake, full-wake, or freestream conditions. In the 25-
turbine wind farm, large jumps in the blade pitch angle, TSR, and yaw set points occur due to small wind direction changes of
approximately $2^\circ - 3^\circ$. Additionally, the behavior in deep turbine arrays is difficult to predict using common wake superposition
methods, particularly when including the effects of wake steering combined with ABL shear and turbulence. These factors
715 combined may make it challenging to achieve the precision necessary for optimal implementation of joint yaw-induction
control strategies, requiring further research in optimization under uncertainty of wind farm flow control.

This study does not account for changes in structural loads caused by applying wind farm control strategies. Structural
loading can increase for certain turbines when wind farm control is in use, and therefore the expected power gain must be
balanced with any potential reduction in turbine lifetime, especially when dealing with large yaw misalignment angles or
720 increased thrust (Van Dijk et al., 2017; Braunbehrens et al., 2024). It is an open question as to what additional benefits joint yaw-
induction control may offer, relative to wake steering alone, in settings of multi-objective optimization accounting for energy
production and loads. To incorporate fatigue damage into control optimization, gradient-compatible fatigue load surrogate
models can be utilized (Riva et al., 2020; Liew et al., 2023a).

It is important to note that the models and conclusions presented in this study are largely applicable to below-rated turbine
725 operation. Although the study can be extended to above-rated conditions, existing literature indicates that the greatest value
of wind farm control is found in low wind speed regions. In these conditions, the value of energy production is highest, and
turbines have the capability to increase their collective power output.

6 Conclusions

In this study, we investigate the opportunities and potential benefits of joint yaw-induction wind farm control (termed *joint*
730 *control*) compared with *yaw control* (wake steering) and *thrust control* (derating or induction control) in isolation. In *joint*
control, the yaw-misalignment angle of a turbine rotor is varied in conjunction with its thrust coefficient. The opportunity for



joint control is revealed through the Unified Momentum Model (Liew et al., 2024a) for wind turbine rotors, which extends classical theory to predict induction, thrust, power, and initial wake velocities under both misalignment and arbitrary thrust coefficients without corrections. The initial wake velocities predicted by the Unified Momentum Model are naturally coupled with widely-used engineering wake models such as the Jensen (Jensen, 1983) or Gaussian (Bastankhah and Porté-Agel, 2014) wake models to ensure consistency between the thrust-yaw relationship, power-yaw relationship, and the wakes, which we use to build a new engineering wind farm model. While the local thrust coefficient C'_T can be prescribed directly when using an actuator disk (AD) rotor model, this approach is not applicable to realistic turbines. Therefore, a blade element momentum (BEM) rotor representation, again based on the Unified Momentum Model, is also explored, where a tip speed ratio λ and blade pitch angle θ_p are prescribed instead. This method aligns more closely with realistic wind turbine control inputs. Automatic differentiation is used to enable computationally efficient and robust solutions to the wind farm control optimization problem. Turbine set points evaluated by the engineering wind farm model under *thrust*, *yaw*, and *joint control* strategies are compared against a *no control* baseline, where all turbines operate at their individual power-maximizing set point ($C'_T = 2$, $\gamma = 0$).

The key findings of this study are documented for each subsection:

Two-Turbine Case Study: For a separation distance of $6D$, the two-turbine case study shows that optimal *joint control* set points smoothly transition between *thrust control* in fully waked conditions and *yaw control* in partially waked conditions. As a result, the optimal yaw setpoints are continuous with respect to wind direction, which is not the case with *yaw control* alone, which is discontinuous in full-wake scenarios. The model-predicted power gain from *joint control* is always greater than or equal to *thrust control* and *yaw control* strategies. Large eddy simulation (LES) runs at a wind direction of 3.8° confirm that the global optimal wind farm control strategy requires a combination of yaw and thrust control. While the Unified Momentum Model predictions of leading turbine power match well with LES, the waked turbine power is underpredicted due to the Gaussian wake model's limitations in capturing the three-dimensional curled wake shape.

25-Turbine Case Study: Similar conclusions are drawn from a 25-turbine wind farm case study. Joint optimization of yaw and thrust leads to the greatest increase in wind farm power production predicted by the wind farm model, increasing wind farm energy production by 4.0% above the *no control* baseline when averaged uniformly over all wind directions with $6D$ spacing. Although the power gains diminish as the inter-turbine spacing increases, *joint control* consistently outperforms *yaw* and *thrust control* in isolation, with the most significant benefit observed at approximately $3.3D$ spacing. A single wind direction of 2.5° was simulated in LES, for which the difference between wind farm power production under *joint* and *yaw control* is statistically indistinguishable, with both achieving power increases over standard greedy individual control of approximately 18% for the wind farm configuration investigated here. As with the two-turbine case, the predictions of the freestream wind turbine power are reliable for the different thrust coefficients and yaw misalignments used in the LES. However, the wind farm model underpredicts the benefit of wind farm control realized in LES at the simulated wind direction due to compounding underestimation in the power produced by downstream turbines waked by yawed upstream turbines. Therefore, the engineering wind farm model is not able to reliably predict the power gain in LES, and is also likely not predicting the true globally optimum control strategy for the 25-turbine wind farm.



Optimal Control Strategy: We show that the optimal choice of tip speed ratio and blade pitch to achieve a particular amount of power derating approximately follows a thrust-minimizing trajectory. The thrust-minimizing trajectory changes with turbine yaw misalignment and is turbine-specific. This conclusion was enabled by the Unified Momentum Model, which can accurately model the relationship between power, thrust, and yaw misalignment of a rotor in both AD and BEM modeling approaches.

770 **Future Work:** Future work should target the development and implementation of computationally efficient, gradient-enabled wind farm flow models that can capture the three-dimensional structure of yawed wind turbines, secondary wake steering, and wake superposition, building on initial research in the literature (Martínez-Tossas et al., 2021; Bastankhah et al., 2022; Narasimhan et al., 2022, 2024). These more advanced wake models can be coupled to the wake initial conditions from the Unified Momentum Model (Liew et al., 2024a). The wake models can also be extended to account for blockage and farm-
775 level entrainment (Stevens et al., 2015; Howland et al., 2020a; Devesse et al., 2024; Ndindayino et al., 2025; Kirby et al., 2025), as there is likely to be an interaction between wind farm flow control and wind plant blockage (Bossanyi and Bleeg, 2024). These improved wake models are necessary to motivate new field campaigns and harness the untapped potential of *joint yaw-induction control* in flow control of wind farms.

Appendix A: Optimized wind farm set points

780 This appendix contains individual turbine thrust and yaw set points (C'_T, γ) for the four wind farm control strategies: *no control*, *thrust control*, *yaw control*, and *joint control*. The optimal parameters are constrained by each control strategy through the fixed and free variables outlined in Table 1.

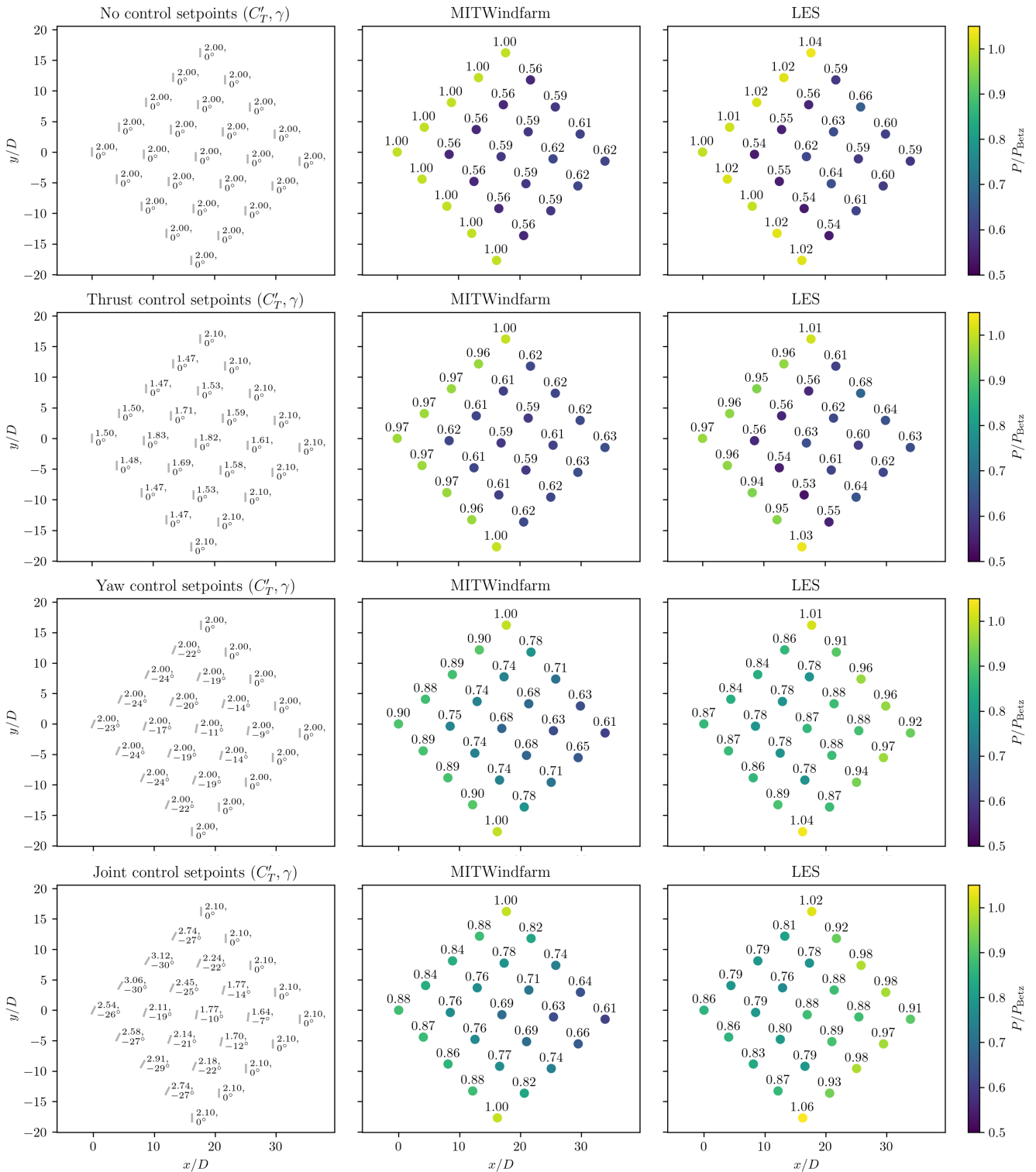


Figure A1. AD set points for the 5×5 turbine array and comparison between farm power in the wind farm flow model and LES.



Code and data availability. Code for the open-source engineering wind farm model, MITWindfarm, is available at <https://doi.org/10.5281/zenodo.15367720> (Liew et al., 2025). The Unified Momentum Model is available as an open-source Python library at <https://doi.org/10.5281/zenodo.10524066> (Liew et al., 2023b), with the rotor modeling package MITRotor at <https://github.com/Howland-Lab/MITRotor>. Model and large eddy simulation data and analysis for the figures in this paper can be found at https://github.com/jaimeliew1/WES2024_Joint_Yaw_Induction. Automatic differentiation was performed using the Dualitic package (<https://github.com/jaimeliew1/Dualitic>). The open-source large eddy simulation code PadéOps is available at <https://github.com/Howland-Lab/PadeOps>.

Author contributions. M.F.H., J.L., and K.S.H. conceived the research. J.L., K.S.H., and I.M.L.U. developed the code. J.L., K.S.H., and I.M.L.U. analyzed the data. K.S.H. performed the large eddy simulations. All authors contributed to manuscript writing and edits.

Competing interests. The authors declare that they have no conflict of interest.

Acknowledgements. K.S.H. and M.F.H. acknowledge funding from the National Science Foundation (Fluid Dynamics program, grant number FD-2226053, Program Manager: Dr. Ronald D. Joslin). J.L. acknowledges support from Siemens Gamesa Renewable Energy. K.S.H. acknowledge additional funding through a National Science Foundation Graduate Research Fellowship under grant no. DGE-2141064. I.M.L.U. acknowledges funding through a MathWorks Fellowship. Simulations were performed on the Stampede3 supercomputer under the NSF ACCESS project ATM170028.



References

- Ali, K., Stallard, T., and Ouro, P.: A Diffusion-Based Wind Turbine Wake Model, *Journal of Fluid Mechanics*, 1001, A13, <https://doi.org/10.1017/jfm.2024.1077>, 2024.
- 800 Allaerts, D. and Meyers, J.: Large eddy simulation of a large wind-turbine array in a conventionally neutral atmospheric boundary layer, *Physics of Fluids*, 27, 2015.
- Annoni, J., Gebraad, P. M. O., Scholbrock, A. K., Fleming, P. A., and van Wingerden, J.-W.: Analysis of Axial-Induction-Based Wind Plant Control Using an Engineering and a High-Order Wind Plant Model, *Wind Energy*, 19, 1135–1150, <https://doi.org/10.1002/we.1891>, 2016.
- Bastankhah, M. and Porté-Agel, F.: A New Analytical Model for Wind-Turbine Wakes, *Renewable Energy*, 70, 116–123, <https://doi.org/10.1016/j.renene.2014.01.002>, 2014.
- 805 Bastankhah, M. and Porté-Agel, F.: Experimental and Theoretical Study of Wind Turbine Wakes in Yawed Conditions, *Journal of Fluid Mechanics*, 806, 506–541, <https://doi.org/10.1017/jfm.2016.595>, 2016.
- Bastankhah, M. and Porté-Agel, F.: Wind tunnel study of the wind turbine interaction with a boundary-layer flow: Upwind region, turbine performance, and wake region, *Physics of Fluids*, 29, 2017.
- 810 Bastankhah, M., Shapiro, C. R., Shamsoddin, S., Gayme, D. F., and Meneveau, C.: A Vortex Sheet Based Analytical Model of the Curled Wake behind Yawed Wind Turbines, *Journal of Fluid Mechanics*, 933, A2, <https://doi.org/10.1017/jfm.2021.1010>, 2022.
- Baydin, A. G., Pearlmutter, B. A., Radul, A. A., and Siskind, J. M.: Automatic Differentiation in Machine Learning: A Survey, *Journal of Machine Learning Research*, 18, 1–43, 2018.
- Bleeg, J., Purcell, M., Ruisi, R., and Traiger, E.: Wind farm blockage and the consequences of neglecting its impact on energy production, *Energies*, 11, 1609, 2018.
- 815 Blondel, F. and Cathelain, M.: An Alternative Form of the Super-Gaussian Wind Turbine Wake Model, *Wind Energy Science*, 5, 1225–1236, <https://doi.org/10.5194/wes-5-1225-2020>, 2020.
- Bossanyi, E.: Combining induction control and wake steering for wind farm energy and fatigue loads optimisation, in: *Journal of Physics: Conference Series*, vol. 1037, p. 032011, IOP Publishing, 2018.
- 820 Bossanyi, E. and Bleeg, J.: How do wind farm blockage and axial induction control interact?, in: *Journal of Physics: Conference Series*, vol. 2767, p. 092027, IOP Publishing, 2024.
- Branlard, E.: *Wind turbine aerodynamics and vorticity-based methods: Fundamentals and recent applications*, 2017.
- Braunbehrens, R., Anand, A., Campagnolo, F., and Bottasso, C.: First experimental results on lifetime-aware wind farm control, in: *Journal of Physics: Conference Series*, vol. 2767, p. 032042, IOP Publishing, 2024.
- 825 Bücker, M.: *Automatic differentiation: applications, theory, and implementations*, Springer, 2006.
- Burton, T., Jenkins, N., Sharpe, D., and Bossanyi, E.: *Wind energy handbook*, John Wiley & Sons, 2011.
- Calaf, M., Meneveau, C., and Meyers, J.: Large Eddy Simulation Study of Fully Developed Wind-Turbine Array Boundary Layers, *Physics of Fluids*, 22, 015 110, <https://doi.org/10.1063/1.3291077>, 2010.
- Cossu, C.: Wake Redirection at Higher Axial Induction, *Wind Energy Science*, 6, 377–388, <https://doi.org/10.5194/wes-6-377-2021>, 2021.
- 830 Crespo, A. and Hernández, J.: Turbulence Characteristics in Wind-Turbine Wakes, *Journal of Wind Engineering and Industrial Aerodynamics*, 61, 71–85, [https://doi.org/10.1016/0167-6105\(95\)00033-X](https://doi.org/10.1016/0167-6105(95)00033-X), 1996.
- Croce, A., Cacciola, S., and Isella, F.: Combining wake redirection and derating strategies in a load-constrained wind farm power maximization, *Wind Energy Science*, 9, 1211–1227, 2024.



- 835 Debuscher, C. M. J., Göçmen, T., and Andersen, S. J.: Probabilistic surrogates for flow control using combined control strategies, in: *Journal of Physics: Conference Series*, vol. 2265, p. 032110, IOP Publishing, 2022.
- Delvaux, T., Van Der Laan, M., and Terrapon, V.: A new RANS-based added turbulence intensity model for wind-farm flow modelling., in: *Journal of Physics: Conference Series*, vol. 2767, p. 092089, IOP Publishing, 2024.
- Devesse, K., Lanzilao, L., and Meyers, J.: A meso–micro atmospheric perturbation model for wind farm blockage, *Journal of Fluid Mechanics*, 998, A63, 2024.
- 840 Gaertner, E., Rinker, J., Sethuraman, L., Zahle, F., Anderson, B., Barter, G. E., Abbas, N. J., Meng, F., Bortolotti, P., Skrzypinski, W., et al.: IEA wind TCP task 37: definition of the IEA 15-megawatt offshore reference wind turbine, Tech. rep., National Renewable Energy Lab.(NREL), Golden, CO (United States), 2020.
- Galinos, C., Larsen, T. J., and Mirzaei, M.: Impact on Wind Turbine Loads from Different down Regulation Control Strategies, *Journal of Physics: Conference Series*, 1104, 012 019, <https://doi.org/10.1088/1742-6596/1104/1/012019>, 2018.
- 845 Gebraad, P., Teeuwisse, F., Van Wingerden, J., Fleming, P. A., Ruben, S., Marden, J., and Pao, L.: Wind plant power optimization through yaw control using a parametric model for wake effects—a CFD simulation study, *Wind Energy*, 19, 95–114, 2016.
- Glauert, H.: The Analysis of Experimental Results in the Windmill Brake and Vortex Ring States of an Airscrew, Tech. Rep. 1026, ARCR R&M, 1926.
- Guirguis, D., Romero, D. A., and Amon, C. H.: Toward Efficient Optimization of Wind Farm Layouts: Utilizing Exact Gradient Information, *Applied Energy*, 179, 110–123, <https://doi.org/10.1016/j.apenergy.2016.06.101>, 2016.
- 850 Heck, K. S. and Howland, M. F.: Coriolis Effects on Wind Turbine Wakes across Neutral Atmospheric Boundary Layer Regimes, *Journal of Fluid Mechanics*, 1008, A7, <https://doi.org/10.1017/jfm.2025.35>, 2025.
- Heck, K. S., Johlas, H. M., and Howland, M. F.: Modelling the induction, thrust and power of a yaw-misaligned actuator disk, *Journal of Fluid Mechanics*, 959, A9, 2023.
- 855 Heck, K. S., Liew, J., and Howland, M. F.: Investigation of far-wake models coupled with yaw-induction control for power optimization, in: *Journal of Physics: Conference Series*, vol. 2767, p. 092103, IOP Publishing, 2024.
- Hosseini, A., Cannon, D. T., and Vassel-Be-Hagh, A.: Wind Farm Active Wake Control via Concurrent Yaw and Tip-Speed Ratio Optimization, *Applied Energy*, 377, 124 625, <https://doi.org/10.1016/j.apenergy.2024.124625>, 2025.
- Houck, D. R.: Review of wake management techniques for wind turbines, *Wind Energy*, 25, 195–220, 2022.
- 860 Howland, M. F., Bossuyt, J., Martínez-Tossas, L. A., Meyers, J., and Meneveau, C.: Wake Structure in Actuator Disk Models of Wind Turbines in Yaw under Uniform Inflow Conditions, *Journal of Renewable and Sustainable Energy*, 8, 043 301, <https://doi.org/10.1063/1.4955091>, 2016.
- Howland, M. F., Lele, S. K., and Dabiri, J. O.: Wind farm power optimization through wake steering, *Proceedings of the National Academy of Sciences*, 116, 14 495–14 500, 2019.
- 865 Howland, M. F., Ghate, A. S., and Lele, S. K.: Influence of the geostrophic wind direction on the atmospheric boundary layer flow, *Journal of Fluid Mechanics*, 883, A39, 2020a.
- Howland, M. F., González, C. M., Martínez, J. J. P., Quesada, J. B., Larranaga, F. P., Yadav, N. K., Chawla, J. S., and Dabiri, J. O.: Influence of atmospheric conditions on the power production of utility-scale wind turbines in yaw misalignment, *Journal of Renewable and Sustainable Energy*, 12, 2020b.
- 870 Howland, M. F., Ghate, A. S., Quesada, J. B., Pena Martínez, J. J., Zhong, W., Larrañaga, F. P., Lele, S. K., and Dabiri, J. O.: Optimal closed-loop wake steering—Part 2: Diurnal cycle atmospheric boundary layer conditions, *Wind Energy Science*, 7, 345–365, 2022a.



- Howland, M. F., Quesada, J. B., Martínez, J. J. P., Larrañaga, F. P., Yadav, N., Chawla, J. S., Sivaram, V., and Dabiri, J. O.: Collective Wind Farm Operation Based on a Predictive Model Increases Utility-Scale Energy Production, *Nature Energy*, <https://doi.org/10.1038/s41560-022-01085-8>, 2022b.
- 875 IEA: Net Zero by 2050, IEA, Paris, 2021.
- IRENA: World Energy Transitions Outlook 2022: 1.5°C Pathway, International Renewable Energy Agency, Abu Dhabi, 2022.
- Jensen, N. O.: A note on wind generator interaction, Risø National Laboratory, 1983.
- Jiménez, Á., Crespo, A., and Migoya, E.: Application of a LES technique to characterize the wake deflection of a wind turbine in yaw, *Wind Energy*, 13, 559–572, 2010.
- 880 Juangarcia, D. A., Eguinoa, I., and Knudsen, T.: Derating a single wind farm turbine for reducing its wake and fatigue, in: *Journal of Physics: Conference Series*, vol. 1037, p. 032039, IOP Publishing, 2018.
- Kheirabadi, A. C. and Nagamune, R.: A quantitative review of wind farm control with the objective of wind farm power maximization, *Journal of Wind Engineering and Industrial Aerodynamics*, 192, 45–73, 2019.
- Kirby, A., Nishino, T., Lanzilao, L., Dunstan, T. D., and Meyers, J.: Turbine-and farm-scale power losses in wind farms: an alternative to
885 wake and farm blockage losses, *Wind Energy Science*, 10, 435–450, 2025.
- Klemmer, K. S. and Howland, M. F.: Momentum deficit and wake-added turbulence kinetic energy budgets in the stratified atmospheric boundary layer, *Physical Review Fluids*, 9, 114 607, 2024.
- Kölle, K., Göçmen, T., Eguinoa, I., Alcayaga Román, L. A., Aparicio-Sanchez, M., Feng, J., Meyers, J., Pettas, V., and Sood, I.: FarmConnors market showcase results: wind farm flow control considering electricity prices, *Wind Energy Science*, 7, 2181–2200, 2022.
- 890 Liew, J., Riva, R., and Göçmen, T.: Efficient Mann turbulence generation for offshore wind farms with applications in fatigue load surrogate modelling, in: *Journal of Physics: Conference Series*, vol. 2626, p. 012050, IOP Publishing, 2023a.
- Liew, J., S. Heck, K., and Howland, M. F.: Unified Momentum Model v0.3.0, Zenodo, <https://doi.org/10.5281/zenodo.10524067>, 2023b.
- Liew, J., Heck, K., and Howland, M.: Unified momentum model for rotor aerodynamics across operating regimes, *Nature Communications*, 15, 6658, <https://doi.org/10.1038/s41467-024-50756-5>, 2024a.
- 895 Liew, J., Heck, K., and Howland, M. F.: Enhanced Modeling of Joint Yaw and Axial Induction Control Using Blade Element Momentum Methods, in: *Journal of Physics: Conference Series*, vol. 2767, p. 032018, IOP Publishing, 2024b.
- Liew, J., Upfal, I. M. L., Heck, K. S., and Howland, M. F.: MITWindfarm v1.0.0, Zenodo, 2025.
- Lio, W. H., Mirzaei, M., and Larsen, G. C.: On wind turbine down-regulation control strategies and rotor speed set-point, in: *Journal of Physics: Conference Series*, vol. 1037, p. 032040, IOP Publishing, 2018.
- 900 Liu, L., Gadde, S. N., and Stevens, R. J.: Geostrophic Drag Law for Conventionally Neutral Atmospheric Boundary Layers Revisited, *Quarterly Journal of the Royal Meteorological Society*, 147, 847–857, <https://doi.org/10.1002/qj.3949>, 2021.
- Maclaurin, D., Duvenaud, D., and Adams, R. P.: Autograd: Effortless Gradients in Numpy, in: *ICML 2015 AutoML Workshop*, vol. 238, p. 5, 2015.
- Martínez-Tossas, L. A., King, J., Quon, E., Bay, C. J., Mudafort, R., Hamilton, N., Howland, M. F., and Fleming, P. A.: The Curled Wake
905 Model: A Three-Dimensional and Extremely Fast Steady-State Wake Solver for Wind Plant Flows, *Wind Energy Science*, 6, 555–570, <https://doi.org/10.5194/wes-6-555-2021>, 2021.
- Martínez-Tossas, L. A., Branlard, E., Shaler, K., Vijayakumar, G., Ananthan, S., Sakievich, P., and Jonkman, J.: Numerical Investigation of Wind Turbine Wakes under High Thrust Coefficient, *Wind Energy*, 25, 605–617, <https://doi.org/10.1002/we.2688>, 2022.



- Medici, D.: Experimental Studies of Wind Turbine Wakes – Power Optimisation and Meandering, Ph.D. thesis, KTH Royal Institute of
910 Technology, Stockholm, Sweden, 2005.
- Meyers, J., Bottasso, C., Dykes, K., Fleming, P., Gebraad, P., Giebel, G., Göçmen, T., and Van Wingerden, J.-W.: Wind farm flow control:
prospects and challenges, *Wind Energy Science Discussions*, 2022, 1–56, 2022.
- Munters, W. and Meyers, J.: Dynamic strategies for yaw and induction control of wind farms based on large-eddy simulation and optimiza-
tion, *Energies*, 11, 177, 2018.
- 915 Narasimhan, G., Gayme, D. F., and Meneveau, C.: Effects of wind veer on a yawed wind turbine wake in atmospheric boundary layer flow,
Physical Review Fluids, 7, 114 609, 2022.
- Narasimhan, G., Gayme, D. F., and Meneveau, C.: An extended analytical wake model and applications to yawed wind turbines in atmo-
spheric boundary layers with different levels of stratification and veer, arXiv preprint arXiv:2412.02216, 2024.
- Ndindayino, O., Puel, A., and Meyers, J.: Effect of blockage on wind turbine power and wake development, *Wind Energy Science Discus-*
920 *sions*, 2025, 1–24, 2025.
- Niyayifar, A. and Porté-Agel, F.: Analytical modeling of wind farms: A new approach for power prediction, *Energies*, 9, 741, 2016.
- Nishino, T. and Draper, S.: Local Blockage Effect for Wind Turbines, *Journal of Physics: Conference Series*, 625, 012 010,
<https://doi.org/10.1088/1742-6596/625/1/012010>, 2015.
- Nordström, J., Nordin, N., and Henningson, D.: The Fringe Region Technique and the Fourier Method Used in the Di-
925 rect Numerical Simulation of Spatially Evolving Viscous Flows, *SIAM Journal on Scientific Computing*, 20, 1365–1393,
<https://doi.org/10.1137/S1064827596310251>, 1999.
- Nygaard, N. G., Steen, S. T., Poulsen, L., and Pedersen, J. G.: Modelling Cluster Wakes and Wind Farm Blockage, *Journal of Physics:*
Conference Series, 1618, 062 072, <https://doi.org/10.1088/1742-6596/1618/6/062072>, 2020.
- Pedersen, J., Svensson, E., Poulsen, L., and Nygaard, N.: Turbulence Optimized Park model with Gaussian wake profile, in: *Journal of*
930 *Physics: Conference Series*, vol. 2265, p. 022063, IOP Publishing, 2022.
- Pedersen, M. M. and Larsen, G. C.: Integrated wind farm layout and control optimization, *Wind Energy Science*, 5, 1551–1566, 2020.
- Pedersen, M. M., Meyer Forsting, A., van der Laan, P., Riva, R., Alcayaga Román, L. A., Criado Risco, J., Friis-Møller, M., Quick, J.,
Christiansen, J. P. S., Valotta Rodrigues, R., Olsen, B. T., and Réthoré, P.-E.: PyWake 2.5.0: An Open-Source Wind Farm Simulation Tool,
2023.
- 935 Peña, J. I., Rodriguez, R., and Mayoral, S.: Cannibalization, depredation, and market remuneration of power plants, *Energy Policy*, 167,
113 086, 2022.
- Prol, J. L., Steininger, K. W., and Zilberman, D.: The cannibalization effect of wind and solar in the California wholesale electricity market,
Energy Economics, 85, 104 552, 2020.
- Quick, J., Rethore, P.-E., Mølgaard Pedersen, M., Rodrigues, R. V., and Friis-Møller, M.: Stochastic Gradient Descent for Wind Farm
940 Optimization, *Wind Energy Science*, 8, 1235–1250, <https://doi.org/10.5194/wes-8-1235-2023>, 2023.
- Risco, J. C., van der Laan, M., Pedersen, M., Forsting, A. M., and Réthoré, P.-E.: A RANS-based surrogate model for simulating wind turbine
interaction, in: *Journal of Physics: Conference Series*, vol. 2505, p. 012016, IOP Publishing, 2023.
- Riva, R., Liew, J., Friis-Møller, M., Dimitrov, N., Barlas, E., Réthoré, P.-E., and Beržonskis, A.: Wind farm layout optimization with load
constraints using surrogate modelling, in: *Journal of Physics: Conference Series*, vol. 1618, p. 042035, IOP Publishing, 2020.
- 945 Schreiber, J., Balbaa, A., and Bottasso, C. L.: Brief Communication: A Double-Gaussian Wake Model, *Wind Energy Science*, 5, 237–244,
<https://doi.org/10.5194/wes-5-237-2020>, 2020.



- Sescu, A. and Meneveau, C.: A Control Algorithm for Statistically Stationary Large-Eddy Simulations of Thermally Stratified Boundary Layers: A Control Algorithm for LES of Thermally Stratified Boundary Layers, *Quarterly Journal of the Royal Meteorological Society*, 140, 2017–2022, <https://doi.org/10.1002/qj.2266>, 2014.
- 950 Shapiro, C. R., Gayme, D. F., and Meneveau, C.: Modelling yawed wind turbine wakes: a lifting line approach, *Journal of Fluid Mechanics*, 841, R1, 2018.
- Shapiro, C. R., Gayme, D. F., and Meneveau, C.: Filtered Actuator Disks: Theory and Application to Wind Turbine Models in Large Eddy Simulation, *Wind Energy*, 22, 1414–1420, <https://doi.org/10.1002/we.2376>, 2019a.
- Shapiro, C. R., Starke, G. M., Meneveau, C., and Gayme, D. F.: A wake modeling paradigm for wind farm design and control, *Energies*, 12, 955 2956, 2019b.
- Shukla, P., Skea, J., Slade, R., Al Khourdajie, A., van Diemen, R., McCollum, D., Pathak, M., Some, S., Vyas, P., Fradera, R., et al.: IPCC Climate Change 2022: Mitigation of Climate Change, Contribution of Working Group III to the Sixth Assessment Report of the Intergovernmental Panel on Climate Change, 2022.
- Stevens, R. J., Graham, J., and Meneveau, C.: A Concurrent Precursor Inflow Method for Large Eddy Simulations and Applications to Finite 960 Length Wind Farms, *Renewable Energy*, 68, 46–50, <https://doi.org/10.1016/j.renene.2014.01.024>, 2014.
- Stevens, R. J., Gayme, D. F., and Meneveau, C.: Coupled wake boundary layer model of wind-farms, *Journal of renewable and sustainable energy*, 7, 2015.
- Tamaro, S., Campagnolo, F., and Bottasso, C. L.: On the power and control of a misaligned rotor–beyond the cosine law, *Wind Energy Science*, 9, 1547–1575, 2024.
- 965 Valotta Rodrigues, R., Pedersen, M. M., Schøler, J. P., Quick, J., and Réthoré, P.-E.: Speeding up Large-Wind-Farm Layout Optimization Using Gradients, Parallelization, and a Heuristic Algorithm for the Initial Layout, *Wind Energy Science*, 9, 321–341, <https://doi.org/10.5194/wes-9-321-2024>, 2024.
- Van Der Laan, M., Andersen, S., Réthoré, P.-E., Baungaard, M., Sørensen, J., and Troldborg, N.: Faster wind farm AEP calculations with CFD using a generalized wind turbine model, in: *Journal of Physics: Conference Series*, vol. 2265, p. 022030, IOP Publishing, 2022.
- 970 Van Dijk, M. T., van Wingerden, J.-W., Ashuri, T., and Li, Y.: Wind farm multi-objective wake redirection for optimizing power production and loads, *Energy*, 121, 561–569, 2017.
- Vitulli, J., Larsen, G. C., Pedersen, M., Ott, S., and Friis-Møller, M.: Optimal open loop wind farm control, in: *Journal of Physics: Conference Series*, vol. 1256, p. 012027, IOP Publishing, 2019.
- Zhang, Z., Huang, P., Bitsuamlak, G., and Cao, S.: Analytical Solutions for Yawed Wind-Turbine Wakes with Application to Wind-Farm 975 Power Optimization by Active Yaw Control, *Ocean Engineering*, 304, 117 691, <https://doi.org/10.1016/j.oceaneng.2024.117691>, 2024.
- Zong, H. and Porté-Agel, F.: A momentum-conserving wake superposition method for wind farm power prediction, *Journal of Fluid Mechanics*, 889, A8, 2020.